UNDERSTANDING SOLUTIONS OF THE ANGULAR TEUKOLSKY EQUATION IN THE PROLATE ASYMPTOTIC LIMIT

BY

DANIEL J. VICKERS

A Thesis Submitted to the Graduate Faculty of

WAKE FOREST UNIVERSITY GRADUATE SCHOOL OF ARTS AND SCIENCES

in Partial Fulfillment of the Requirements

for the Degree of

MASTER OF SCIENCE

Physics

December 2020

Winston-Salem, North Carolina

Approved By:

Gregory B. Cook, Ph.D., Advisor

Eric D. Carlson, Ph.D., Chair

Samuel S. Cho, Ph.D.

Table of Contents

List of Figures

List of Tables

Abstract

Solutions of the angular Teukolsky equation are required to obtain frequency-domain solutions for perturbations on the Kerr geometry. The analytic behavior of solutions to the angular Teukolsky equation have been explored in expansions about the spherical limit, and in the asymptotic oblate limit. However, obtaining the general behavior in the asymptotic prolate limit has proven difficult. We perform a high accuracy study of prolate solutions to the angular Teukolsky equation, and use these to extend our understanding of the analytic behavior of solutions in the asymptotic prolate limit. We found two categories of prolate solutions. One group of solutions, which we call non-anomalous solutions, are in agreement with solutions previously predicted and calculated numerically. The second category of prolate solutions, which we call anomalous solutions, to the best of our knowledge, are a previously unknown set of solutions for the prolate case. The existence of the anomalous solutions strongly affects the transition of the non-anomalous solutions to their asymptotic limit. Based on our understanding of the anomalous solutions, we have extended the polynomial fit of the non-anomalous solutions to higher order than any previous numerical studies. We similarly determined a limited polynomial fit for the anomalous solutions and explored their basic properties. Our hope is that these solutions will provide clarity to, and reduce the computational load on, future studies which require solutions to the angular Teukolsky equation.

Introduction

Perturbation theory is of great use in mathematical physics. When solving a complicated problem, one can start with the known solutions to a similar and simpler problem and solve for the correction on the simpler solutions due to a small perturbation.

In gravitation, this is commonly done by adding a perturbation to the metric of space-time. One can start with a well-understood metric, $g_{\mu\nu}$, and add a small perturbation, $h_{\mu\nu}$, such that the full metric of interest is $g'_{\mu\nu} = g_{\mu\nu} + h_{\mu\nu}$. By expanding the field equations to first order in $h_{\mu\nu}$, one may derive partial differential wave equations which are linearized approximations of solutions on $g'_{\mu\nu}$ with respect to the perturbation. The Schwarzschild metric is a relatively simple and well-understood metric in which we do not account for any angular momentum of a compact object. For the Schwarzschild metric, perturbation theory can be used to linearize the Einstein equation and leads to a differential equation which is separable, called the Regge-Wheeler equation[25]. The Regge-Wheeler equation is a Schrödinger-type equation for odd-parity perturbations on the Schwarzschild metric. Later, Zerilli[30] extended this equation to include even-parity perturbations into what is known as the Zerilli equation. Bardeen and Press[2] derived a single master equation for scalar, electromagnetic, and gravitational perturbations on the Schwarzschild metric called the Bardeen-Press equation.

While the Schwarzschild solution is a useful approximation for the case of slowly-rotating black holes, one can expect a typical black hole to have significant angular momentum and therefore be rotating too quickly to accurately be approximated by the Schwarzschild metric. Thus a more accurate and general metric to find linearizations on would include the rotational behavior of black holes. A common choice for such a metric is the Kerr metric, since it is asymptotically flat. The Kerr metric, is given as

$$\begin{aligned} ds^2 = &-\left(1-\frac{2Mr}{\Sigma}\right)dt^2 - \left(\frac{4Mar\,\sin^2\theta}{\Sigma}\right)dtd\phi \\ &+\frac{\Sigma}{\Delta}dr^2 + \Sigma d\theta^2 + \sin^2\theta\left(r^2+a^2+\frac{2Ma^2r\,\sin^2\theta}{\Sigma}\right)d\phi^2. \end{aligned} \tag{0.1}$$

Here $\Sigma = r^2 + a^2\cos^2\theta$, $\Delta = r^2 - 2Mr + a^2$, and $a = \frac{J}{M}$ is the angular momentum per unit mass. Linearizations of the Einstein equation in a Kerr geometry are generally more complex to solve both analytically and numerically than those of the Schwarzschild geometry. The first attempt to linearize the Einstein equation for a Kerr metric which lead to separable equations was performed by Teukolsky[28]. In Ref. [28], Teukolsky utilized the Newman-Penrose formalism to derive a completely separable equation for perturbations on the Kerr metric. This equation,

$$
\begin{aligned}
4\pi\Sigma T = & \left[\frac{(r^2+a^2)^2}{\Delta} - a^2\sin^2\theta\right]\frac{\partial^2\psi}{\partial t^2} + \frac{4Mar}{\Delta}\frac{\partial^2\psi}{\partial t\partial\phi} + \left[\frac{a^2}{\Delta} - \frac{1}{\sin^2\theta}\right]\frac{\partial^2\psi}{\partial\phi^2} \\
& - \Delta^{-s}\frac{\partial}{\partial r}\left(\Delta^{s+1}\frac{\partial\psi}{\partial r}\right) - \frac{1}{\sin\theta}\frac{\partial}{\partial\theta}\left(\sin\theta\frac{\partial\psi}{\partial\theta}\right) - 2s\left[\frac{a(r-M)}{\Delta} + \frac{i\cos\theta}{\sin^2\theta}\right]\frac{\partial\psi}{\partial\phi} \\
& - 2s\left[\frac{M\left(r^2-a^2\right)}{\Delta} - r - ia\cos\theta\right]\frac{\partial\psi}{\partial t} + \left(s^2\cot^2\theta - s\right)\psi,
\end{aligned}
\tag{0.2}
$$

is known as the Teukolsky master equation. Here T is related to the stress energy tensor. In the vacuum case, $T = 0$ and Eq. (0.2) can be separated by making the substitution $\psi = e^{-i\omega t}e^{im\phi}\,{}_sS_{\ell m}(\theta)R(r)$. The angular and radial components of the equation are ${}_sS_{\ell m}$ and R respectively. We refer to ${}_sS_{\ell m}e^{im\phi}$ as the spin-weighted spheroidal harmonics (SWSHs) and ${}_sS_{\ell m}$ as the spin-weighted spheroidal function. The usefulness in Eq. (0.2) is in that this one equation can apply to all fields via a choice of s. For example, scalar-valued fields use spin $s = 0$, spin-half fields use $s = \pm\frac{1}{2}$, electric fields use values of $s = \pm 1$, and gravitational fields use $s = \pm 2$. For gravitational fields with spin $s = \pm 2$, ψ is related to components of the Weyl tensor. For a full description of ψ for values of s, refer to table 1 of Ref. [28].

To solve Eq. (0.2), one typically must solve for solutions with respect to the mode frequency, ω. Solutions in terms of ω are called frequency-domain solutions. Most work has been done in the frequency domain since these solutions are generally easier to work with and are typically more accurate. If necessary, frequency-domain solutions can always be converted into solutions with respect to the time variable, t, by use of Fourier transform.

Arriving at time-domain solutions tends to be more computationally expensive when converting the frequency-domain solutions into time-domain solutions. To reduce computational load, there has been some work to directly solve Eq. (0.2) in the time domain. Krivan, Laguna, Papadopoulos, and Andersson[17] developed a 2+1 PDE method to solve Eq. (0.2) for time-domain solutions of a point mass perturbation near a Kerr black hole. Using the same 2+1 PDE method, Lopez-Aleman, Khanna,and Pullin[20] solved for the gravitational radiation of a particle with Gaussian mass distribution using time evolution. Nakano, Zlochower, Lousto, and Campanelli[22] used time-domain evolution methods along with solutions to Eq. (0.2) to solve for trajectories of intermediate mass-ratio black hole binaries, with $q = 1/10$, $q = 1/15$, and $q = 1/100$, where $q = \frac{M_1}{M_2}$ is the ratio of the masses in a binary system.

In the extreme mass-ratio limit, one assumes that one object's mass is significantly smaller than that of the object such that $q \to 0$. One of the earliest uses of Eq. (0.2) was by Bardeen, Press, and Teukolsky[3] to model the synchrotron radiation of a charged point mass of extreme mass-ratio moving in a Kerr background for frequency-domain solutions by treating the point mass as a perturbation in the geometry.

Equation (0.2) includes a long-ranged potential, meaning that the behavior of the radial equation is determined by the behavior of the potential at spatial infinity. Equation (0.2) is often converted into short ranged forms for certain problems. Detweiler and Chandrasekhar[12] solved for a short-ranged real-potential transformation of Eq. (0.2) in the case that the spin-weight $s = -2$. Around the same time, Chandrasekhar[9] derived relations between Eq. (0.2) and the Bardeen-Press equation, Regge-Wheeler equation, and Zerilli equation. The transformations in Ref. [12] were the precursor to work by Sasaki and Nakamura[26] to develop the Sasaki-Nakamura-Teukolsky formalism to help convert between general short-ranged field equations and Eq. (0.2). Sasaki and Nakamura used this formalism to compute frequency-domain solutions for gravitational radiation when using the perturbation of a point-mass falling into a Kerr black hole from spatial infinity.

Hughes[16] used Eq. (0.2) with the Sasaki-Nakamura-Teukolsky formalism to numerically calculate the change in the energy, angular momentum, and Carter constant of a non-equatorial orbiting point mass perturbation near a Kerr black hole. Hughes was able to calculate the energy and angular momentum radiated to infinity. Similar works using Eq. (0.2) to solve for gravitational radiation have been of great interest as of late due to their relevance in the interpretation of gravitational wave observations from LIGO, VIRGO, and eventually LISA.

Equation (0.2) is also commonly used in the study of modes of Kerr. These modes are fundamental resonances on the space-time and are defined by their boundary conditions. For a Kerr geometry, these boundaries are the event horizon of the black hole and spatial infinity. For many situations, we want to find solutions which do not allow waves to emit from the black hole nor to enter the system at spatial infinity. The modes which satisfy these boundary conditions are called quasi-normal modes

(QNMs). In the case of gravitational radiation from compact objects like black holes, the QNMs that are present in the ringdown signal allow us to determine properties of the source such as angular momentum and mass and have already been used with recent gravitational wave observations[1]. One must solve for QNMs of Kerr black holes by simultaneously solving the radial and angular parts of Eq. (0.2).

Ferrari and Mashhoon[13] made one of the earliest attempts to approximate analytic solutions for QNMs of slowly-rotating Kerr black holes by finding bound states of the inverted Kerr potential for Eq. (0.2). Brink[21] also made progress towards analytic solutions for QNMs in the Schwarzschild limit. While there has been significant work in solving QNMs for non-rotating black holes by use of Green's functions[23, 27], no such method has of yet been generalized for rotating black holes.

Leaver's method[19] is one of the earliest numerical methods for use with Eq. (0.2) to solve for Kerr QNMs, and has become one of the most broadly used algorithms available to solve Eq. (0.2) numerically. Leaver derived this method by converting the radial and angular parts of Eq. (0.2) into infinite continued fractions, which Leaver truncated at a finite depth and solved. Onozawa[24] used Leaver's method to solve for highly-damped modes of Kerr. Berti, Cardoso, and Casals[4] used Leaver's method with their own shooting method to compute slowly-damped QNMs to high precision. Of particular note for the work in this paper, Cook and Zalutskiy[11] developed a spectral decomposition method for solving the angular component of Eq. (0.2) while using Leaver's method to solve for the radial component in order to find QNMs of

Kerr.

Total transmission modes (TTMs) are similar to QNMs except they swap one of the boundary conditions. Left TTMs (TTMLs) allow the waveform to travel in from spatial infinity and right TTMs (TTMRs) allow outgoing waves at the black hole event horizon. This naming scheme assumes a picture with the black hole situated to the left and spatial infinity to the right. Cook and Zalutskiy's spectral method was used by Cook, Annichiarico, and Vickers[10] to solve Eq. (0.2) for TTMRs, TTMLs, and QNMs.

By separating out the angular component of Eq. (0.2) and making the substitution $\cos\theta$=x, one is able to express the angular Teukolsky equation as

$$\left[\left(1-x^2\right)\ {}_sS_{\ell m,x}\right]_x + \left[(cx)^2 - 2scx + s + {}_sA_{\ell m} - \frac{(m+sx)^2}{1-x^2}\right] {}_sS_{\ell m} = 0. \qquad (0.3)$$

${}_sA_{\ell m}$ is the angular separation constant, which is treated as the eigenvalue when solving Eq. (0.3) with the eigenfunction being ${}_sS_{\ell m}$. For simplicity, we have set $a\omega = c$. We refer to c as the oblateness parameter. When $s = 0$ and c is purely real or imaginary, Eq. (0.3) is obtained from separating the Laplacian in spheroidal coordinates and c specifies the oblateness or prolateness of the coordinates. For Eq. (0.3), values of c that are purely real are referred to as oblate, and values such that $ic \in \Re$ are prolate. In general the value of c is complex. Due to greater simplicity, most works to arrive at analytic solutions for Eq. (0.3) are focused on the purely oblate or purely prolate cases.

We refer to m as the azimuthal index. There are countably infinite solutions to Eq. (0.3) for any given combination of m, s, and c, and we label these solutions with the index ℓ—referred to as the multipole number. For generalized ${}_sS_{\ell m}$, the minimum multipole number $\ell_{min} = \max(|m|, |s|)$. We often define another index $L = \ell - \max(|m|, |s|)$ so that $L_{min} = 0$ for all combinations of m and s.

In the case that $c = 0$, the SWSHs reduce to the well-known spin-weighted spherical harmonics, ${}_sY_{\ell m}$. For $s = c = 0$, Eq. (0.3) becomes the equation for scalar spherical harmonics commonly used in electrostatics and quantum solutions for the state of an atom.

The SWSHs also form a natural basis for several problems outside of the field of gravitation. Figueiredo[14] used the $s = 1$ SWSHs to solve the two-center electron problem. Larsson, Levitina, and Brändas[18] used the prolate $s = 0$ SWSHs to solve various applied problems in signal processing.

A power series expansion in c for ${}_sA_{\ell m}$ has been solved analytically by Breuer, Ryan, and Waller[7] in the small c limit. They also derived an analytic power series expansion in c in the asymptotic limit ($c \gg 1$) for the oblate case. Minor corrections to the oblate power-series solution were added by Casals and Ottewill[8].

An analytic power series for the prolate asymptotic behavior in powers of c of ${}_sA_{\ell m}$ has only been solved in the case of $s = 0$ by Flammer[15]. In the $s = -2$ case for prolate eigenvalues, Ref. [4] numerically solved for spin-weighted spheroidal functions. Ref. [10] found solutions to Eq. (0.3) in the prolate asymptotic limit for the case of $m = 0$ and $s = 2$. In this case, Ref. [10] fit a high-accuracy power-series expansion in powers of $|c|$. In general, solutions for $s \neq 0$ in the asymptotic regime continue to be unsolved.

As a follow-up to Ref. [10], Vickers[29] performed work to arrive at an analytic power-series expansion in c for generalized prolate ${}_sA_{\ell m}$ using the same spectral decomposition method as Ref. [11] to generate numerical solutions on which fits are based. The work in this paper is a direct expansion of Ref. [29] in which we hope to extend the power-series expansion for ${}_sA_{\ell m}$ for the general asymptotic prolate case. Arriving at this power-series expansion will hopefully be useful for future attempts to solve Eqs. (0.3) and (0.2). We have also found information related the odd behavior found by Ref. [4] and we hope it will reveal a possible reason for the difficulty in finding an analytic solution to the Eq. (0.3).

Chapter 1 of this thesis will be an overview of the numerical methods used in this work as well as the basic analytic properties of the spin-weighed spheroidal functions and their eigenvalues. Chapter 2 will be a qualitative analysis of our survey of prolate solutions for ${}_sA_{\ell m}$ and ${}_sS_{\ell m}$ as well as an initial categorization of the data. In Ch. 3, we will compare our numerical solutions to Eq. (0.3) with the analytic solutions for the $s = 0$ case derived in Ref. [15]. Chapter 4 will be an overview of our fitting methods as well as where we will produce numerical fits for one category of the prolate solutions. In Ch. 5, we will explore properties of, and numerically fit, a secondary category of prolate solutions. Chapter 6 will be our concluding remarks on the results in this study.

Chapter 1: Numerically Solving for the Spin-Weighted Spheroidal Functions

In this chapter, we will give an overview of the spin-weighted spheroidal functions. This will include their basic analytic properties and the numerical methods to construct high-accuracy numerical solutions. We will cover our data generation and organization techniques for producing solutions to Eq. (0.3) in the prolate asymptotic limit. We do this so that we may numerically fit the separation constant, ${}_sA_{\ell m}$. In doing so, we make use of some of the known properties of the spin-weighted spheroidal functions and their associated eigenvalues.

The spin-weighted spheroidal functions, ${}_sS_{\ell m}$, and the angular separation constant, ${}_sA_{\ell m}$, are treated as the eigenfunction and eigenvalue of Eq. (0.3) respectively. The values of m and s appear in Eq. (0.3), but the multipole number, ℓ, does not. The multipole number is only used to label the eigensolutions of Eq. (0.3) for a particular combination of m and s. ${}_sS_{\ell m}$ and ${}_sA_{\ell m}$ are purely real in the $s = 0$ or oblate cases, ${}_sA_{\ell m}$ is also purely real in the $m = 0$ case, and both are generally complex otherwise.

The multipole number satisfies $\ell \geq \max(|m|, |s|)$ and $\ell_{min} \equiv \max(|m|, |s|)$. Common practice is to define $L = \ell - \max(|m|, |s|)$. This definition ensures that the minimum value of L for any given combination of m and s is zero. The number of zero crossings of the oblate ${}_sS_{\ell m}$ and for prolate ${}_0S_{\ell m}$ is known to be equal to L. The real component of prolate ${}_sS_{\ell m}$ will have L zero-crossings plus additional real zero-crossings dependent upon the value of $|s|$.

The values of ${}_sA_{\ell m}$ have some symmetries, such that

$$ {}_sA_{\ell m}(c) = {}_sA^*_{\ell(-m)}(-c^*), \tag{1.1} $$

and

$$ {}_{-s}A_{\ell m}(c) = {}_sA_{\ell m}(c) + 2s. \tag{1.2} $$

Equations (1.1) and (1.2) are useful since they allow us to reduce the numerical work when calculating the values of ${}_sA_{\ell m}$. By solving Eq. (0.3) for any given values of m and s, one can immediately recover solutions for $m \to -m$ and $s \to -s$.

In the spherical limit ($c \to 0$), ${}_sS_{\ell m}$ reduces to ${}_sY_{\ell m}$, meaning the eigenvalues of the spin-weighted spheroidal functions reduce to the eigenvalues of the spin-weighted spherical harmonics;

$$ {}_sA_{\ell m}(c=0) = \ell(\ell+1) - s(s+1). \tag{1.3} $$

For the oblate asymptotic limit, Breuer, Ryan, and Waller[7] analytically derived a power-series expansion for ${}_sA_{\ell m}$ which is

$$ {}_sA_{\ell m} = -c^2 + 2{}_sq_{\ell m}c - \frac{1}{2}\left[{}_sq_{\ell m}^2 - m^2 + 2s + 1\right] + \frac{1}{c}A_1 + \frac{1}{c^2}A_2 + O\left(c^{-3}\right), \tag{1.4} $$

where

$$ A_1 = -\frac{1}{8}\left[{}_sq_{\ell m}^3 - m^2\,{}_sq_{\ell m} + {}_sq_{\ell m} - s^2({}_sq_{\ell m} + m)\right], \tag{1.5} $$

and

$$ A_2 = -\frac{1}{64}\left[5\,{}_sq_{\ell m}^4 - \left(6m^2 - 10\right){}_sq_{\ell m}^2 + m^4 - 2m^2 - 4s^2\left({}_sq_{\ell m}^2 - m^2 - 1\right) + 1\right]. \tag{1.6} $$

Using the terms ${}_s\ell_m = \max\left(|m|, |s|\right) + \frac{1}{2}\left(|m+s| - |m-s|\right) + s$ and $z_0 =$

$\frac{1}{2}\left(1+(-1)^{\ell-{}_s\ell_m}\right)$, the value of ${}_sq_{\ell m}$ was derived by Casals and Ottwill[8][1] to be

$$ {}_sq_{\ell m} = L + \frac{|m+s|+|m-s|}{2} + 1 + z_0 \text{ if } \ell \geq \max\left({}_s\ell_m,\ {}_{-s}\ell_m\right), \tag{1.7} $$

or

$$ {}_sq_{\ell m} = 2L + |m \mp s| \mp s + 1 \text{ if } \ell < {}_{\pm s}\ell_m. \tag{1.8} $$

Flammer[15] derived the first asymptotic power-series expansion for prolate ${}_0A_{\ell m}$ in powers of $|c|$. By making the substitution ${}_0S_{\ell m} = \sqrt{1-\frac{x^2}{2|c|}}\,u_{\ell m}$ in the prolate asymptotic limit, Flammer noted that Eq. (0.3) transformed into a differential form similar to the equation for the parabolic cylinder functions

$$ \frac{d^2D_r}{dx^2} + \left(r + \frac{1}{2} - \frac{1}{4}x^2\right) D_r = 0. \tag{1.9} $$

Solutions to Eq. (1.9) have r zeros between the endpoints. Showing that the number of zeros of ${}_0S_{\ell m}$ is constant between the spherical limit and asymptotic limit, and therefore $r = L$, Flammer showed that the power-series solution for the prolate values

[1] The equation for ${}_s\ell_m$ is in the original form in which it was published, but can be simplified to read ${}_s\ell_m = |m+s| + s$.

of ${}_0A_{\ell m}$ is

$$
\begin{aligned}
{}_0A_{\ell m,flammer} =& |c|\left(2L+1\right) - \left(2L^2+2L+3-4m^2\right)2^{-2} \\
& - \frac{1}{|c|}\left(2L+1\right)\left(L^2+L+3-8m^2\right)2^{-4} - \frac{1}{|c|^2}\big[5\left(L^4+2L^3+7L+3\right) \\
& - 48m^2\left(2L^2+2L+1\right)\big]2^{-6} + O\left(|c|^{-3}\right).
\end{aligned}
\tag{1.10}
$$

In the prolate asymptotic limit for general s, Berti, Cardoso, and Casals[5] deduced the leading-order behavior for some ${}_sA_{\ell m}$. For general s, they separated ${}_sS_{\ell m}$ into inner and outer regions, ${}_sS^{inner}_{\ell m}$ and ${}_sS^{outer}_{\ell m}$ respectively. Inner solutions are defined as solutions for the region far from the endpoints of $x = \pm 1$ and are solved almost identically to the method used by Flammer. Note that the transformation used in Ref. [15] assumes that ${}_sS_{\ell m}$ go to zero at the endpoints. Using arguments similar to those in Ref. [15], Berti, Cardoso, and Casals determined that the number of zero crossings of the real component of ${}_sS^{inner}_{\ell m}$ is equal to L and must fall in the region $|x| < \sqrt{\frac{2L+1}{|c|}}$. Outer solutions are solutions of ${}_sS_{\ell m}$ for $1/\sqrt{|c|} \ll |x| < 1$. Berti, Cardoso, and Yoshida[4] calculated the number of zero crossings of the real component of ${}_sS^{outer}_{\ell m}$ by utilizing a WKB approximation in Ref. [8] near $x = \pm 1$ and matching in the overlapping regions of ${}_sS_{\ell m}^{inner}$ and ${}_sS_{\ell m}^{outer}$ to show that

$$
\begin{aligned}
{}_sS_{\ell m}^{outer,\pm 1} =& (-i)^s 2^{L+1/2} (\pm\sqrt{2|c|})^L e^{-3|c|/2} (1-x^2)^{-1/4} x^L \\
& \times (1+\sqrt{1-x^2})^{-L-1/2} (x - i\sqrt{1-x^2})^{-s} e^{|c|\sqrt{1-x^2}}.
\end{aligned}
\tag{1.11}
$$

Finding the zeros of Eq. (1.11) is then straightforward and depends solely upon s. In general, there are no outer zero-crossings for $s = 0, \pm 1$. For ${}_{\pm 2}S_{\ell m}$, there are two real zero crossings near $x = \pm\frac{1}{\sqrt{2}}$, and there are generally real zero-crossings in the outer region for $|s| \geq 2$.

Using the information from the inner solutions, Berti, Cardoso, and Yoshida[4] determined that in the prolate asymptotic limit,

$$
{}_sA_{\ell m} = (2L+1)|c| + O\left(|c|^0\right). \tag{1.12}
$$

Equation (1.12) agrees with previously known numeric solutions to Eq. (0.3), which were found for limited cases[4, 10]. The terms of constant order and smaller in $|c|$ are not known for the prolate asymptotic case, and these terms are what we will be determining in this work with our numerical solutions to Eq. (0.3).

Our method of numerically solving Eq. (0.3) is the same spectral-decomposition approach utilized in Ref. [11]. When using spectral decomposition, one chooses a set of basis functions that span the space of desired solutions. One can then substitute the linear combination of basis functions into the equation being solved. The goal of this substitution is typically to write out some recursion relation with respect to the coefficients of the linear combination. This allows the equation being solved to be converted into a matrix eigenvalue problem which is solved numerically.

A spectral method offers many advantages in our case that are not offered by other algorithms. The spectral method used in Ref. [11] offers a high degree of accuracy and the spectral method will generate multiple eigensolutions each time we solve a given matrix. This makes the spectral approach very computationally efficient for the amount of data we generated.

In the case of Eq. (0.3), Cook and Zalutskiy[11] chose to use the spin-weighted spherical harmonics as the basis functions so that

$$
{}_sS_{\ell m}e^{im\phi} = \sum_{\ell'} C_{\ell'\ell m}\, {}_sY_{\ell' m}. \tag{1.13}
$$

The functions ${}_sY_{\ell m}$ form a complete basis, so we can be sure that ${}_sS_{\ell m}$ is spanned by ${}_sY_{\ell m}$.

Plugging Eq. (1.13) into Eq. (0.3), Ref. [11] then eliminates the x dependence by use of the recursions relation[6] which satisfies

$$x\, {}_sY_{\ell m} = \mathcal{F}_{s\ell m}\, {}_sY_{(\ell+1)m} + \mathcal{G}_{s\ell m}\, {}_sY_{(\ell-1)m} + \mathcal{H}_{s\ell m}\, {}_sY_{\ell m}. \tag{1.14}$$

where

$$\begin{aligned}
\mathcal{F}_{s\ell m} &= \sqrt{\frac{((\ell+1)^2-m^2)}{(2\ell+3)(2\ell+1)}\frac{((\ell+1)^2-s^2)}{(\ell+1)^2}}, \\
\mathcal{G}_{s\ell m} &= \sqrt{\frac{(\ell^2-m^2)}{(4\ell^2-1)}\frac{(\ell^2-s^2)}{\ell^2}} \text{ if } \ell \neq 0, \text{ 0 otherwise, and} \\
\mathcal{H}_{s\ell m} &= -\frac{ms}{\ell(\ell+1)} \text{ if } \ell \neq 0, \text{ 0 otherwise.}
\end{aligned} \tag{1.15}$$

After using Eq. (1.14), Ref. [11] was then able to derive a five-term recursion relation on $C_{\ell'\ell m}$ as

$$\begin{aligned}
0 =& - c^2\mathcal{A}_{s(\ell'-2)m}C_{(\ell'-2)\ell m} - \left[c^2\mathcal{D}_{s(\ell'-1)m} - 2cs\mathcal{F}_{s(\ell'-1)m}\right]C_{(\ell'-1)\ell m} \\
&+ \left[\ell'(\ell'+1) - s(s+1) - c^2\mathcal{B}_{s\ell' m} + 2cs\mathcal{H}_{s\ell' m} - {}_sA_{\ell m}\right]C_{\ell'\ell m} \\
&- \left[c^2\mathcal{E}_{s(\ell'+1)m} - 2cs\mathcal{G}_{s(\ell'+1)m}\right]C_{(\ell'+1)\ell m} - c^2\mathcal{C}_{s(\ell'+2)m}C_{(\ell'+2)\ell m}.
\end{aligned} \tag{1.16}$$

Equation (1.16) makes use of the following coefficients:

$$\begin{aligned}
\mathcal{A}_{s\ell m} &= \mathcal{F}_{s\ell m}\mathcal{F}_{s(\ell+1)m}, \\
\mathcal{B}_{s\ell m} &= \mathcal{F}_{s\ell m}\mathcal{G}_{s(\ell+1)m} + \mathcal{F}_{s(\ell-1)m}\mathcal{F}_{s\ell m} + \mathcal{H}^2_{s\ell m}, \\
\mathcal{C}_{s\ell m} &= \mathcal{G}_{s\ell m}\mathcal{G}_{s(\ell-1)m}, \\
\mathcal{D}_{s\ell m} &= \mathcal{F}_{s\ell m}(\mathcal{H}_{s\ell m} + \mathcal{H}_{s(\ell+1)m}), \\
\mathcal{E}_{s\ell m} &= \mathcal{G}_{s\ell m}(\mathcal{H}_{s(\ell-1)m} + \mathcal{H}_{s\ell m}).
\end{aligned} \tag{1.17}$$

This recursion relation represents an infinite-dimensional pentadiagonal matrix eigenvalue problem where ${}_sA_{\ell m}$ is the eigenvalue. Notice that any given matrix holds constant the values of m, s, and c, and the set of eigensolutions is indexed by ℓ. The eigenvectors will be the coefficients $C_{\ell'\ell m}$ which we combine with Eq. (1.13) to yield ${}_sS_{\ell m}$ for a given ℓ.

To numerically solve this eigenvalue problem, we truncate the matrix at size $n \times n$, and the matrix will span values of $0 \leq \ell' - \max(|m|, |s|) \leq n - 1$. The magnitudes of $C_{\ell' \ell m}$ decrease exponentially with increasing ℓ', for ℓ' that are large enough to be in the convergent regime. This ensures that for a particular value of ℓ and large enough matrix size, contributions to ${}_sS_{\ell m}$ from ${}_sY_{\ell' m}$ will be negligible for values of $\ell' \geq n + \max(|m|, |s|)$. Selecting a range of solutions we were interested in such that $\ell_{min} \leq \ell \leq \ell_{max}$, we confirmed the numerical accuracy of these solutions by checking the last two coefficients, $C_{(n+\max(|m|,|s|)-1)\ell m}$ and $C_{(n+\max(|m|,|s|)-2)\ell m}$, for all ℓ of interest. If any coefficient were found to be larger than an error threshold of $\epsilon \geq 10^{-24}$, the matrix size was expanded and the calculation was repeated until the error was sufficiently small.

We used this algorithm in the asymptotic regime along the negative imaginary axis in c. For each combination of m and s, we solved in the cases of $ic = 10^{\delta}$ for $-5 \leq \delta \leq 5$ in steps of $\Delta\delta = \frac{1}{1000}$.

We first solved Eq. (0.3) near the spherical limit for the particular values of $ic = 10^{-5}$ and $ic = 10^{-4.999}$. We used Eq. (1.3) to determine the expected eigenvalues in the spherical limit based on L. This expectation was matched to our numerical spherical limit solutions which allowed us to label sequences of solutions by values of L. Starting with our two known points in each sequence, we used a linear prediction algorithm to match solutions to Eq. (0.3) for $ic > 10^{-4.999}$ with the spherical limit solutions to form sequences as ic increased. Starting sequences near the spherical limit in this way ensured that our labels of L were consistent with the spherical limit.

Chapter 2: Qualitative Analysis of Eigenvalue Solutions

After generating sequences of solutions, we compared our data with expectation. Equations (1.1) and (1.2) ensure that we need only produce data for the cases of $m \geq 0$ and $s \geq 0$; however, we generated solutions for enough combinations of $m < 0$ and $s < 0$ to ensure our numerical fits obeyed these symmetries. In total, we generated sequences of solutions which were categorized for all integer combinations of $-10 \leq m \leq 20$, $-10 \leq s \leq 20$, and $L \leq 15$[1]. The sequences contained triplets of $(c,\, {}_sA_{\ell m},\, {}_sS_{\ell m})$ for $10^{-5} \leq ic \leq 10^5$.

We want to confirm the behavior stated in Eq. (1.12), which expects a linear leading-order behavior for the real component of ${}_sA_{\ell m}$. Eigensolutions which agree with Eq. (1.12) are also predicted to have ${}_sS_{\ell m}$ with a certain number of real zero-crossings as stated in Ref. [5] for the inner and outer solutions. Namely, we expect L real zero crossings of ${}_sS_{\ell m}$ in the inner region of $\cos^{-1}\left(\sqrt{\frac{2L+1}{|c|}}\right) < \theta < \cos^{-1}\left(-\sqrt{\frac{2L+1}{|c|}}\right)$, and a number of real zero crossing determined by Eq. (1.11) for the outer regions such that $|\theta - \frac{\pi}{2}| \gg \cos^{-1}\left(|c|^{-1/2}\right)$. Specifically, we expect that

[1] In some cases, values of $L > 15$ were also checked.

the $s = 0$ and $s = \pm 1$ cases have no zero-crossings in the outer region of the real components, the $s = \pm 2$ cases have two real zero-crossings at $\theta = \cos^{-1}(\pm 2^{-1/2})$, and so on. The behaviors of the symmetries from Eqs. (1.1) and (1.2) are known exactly, and it is straightforward to show each.

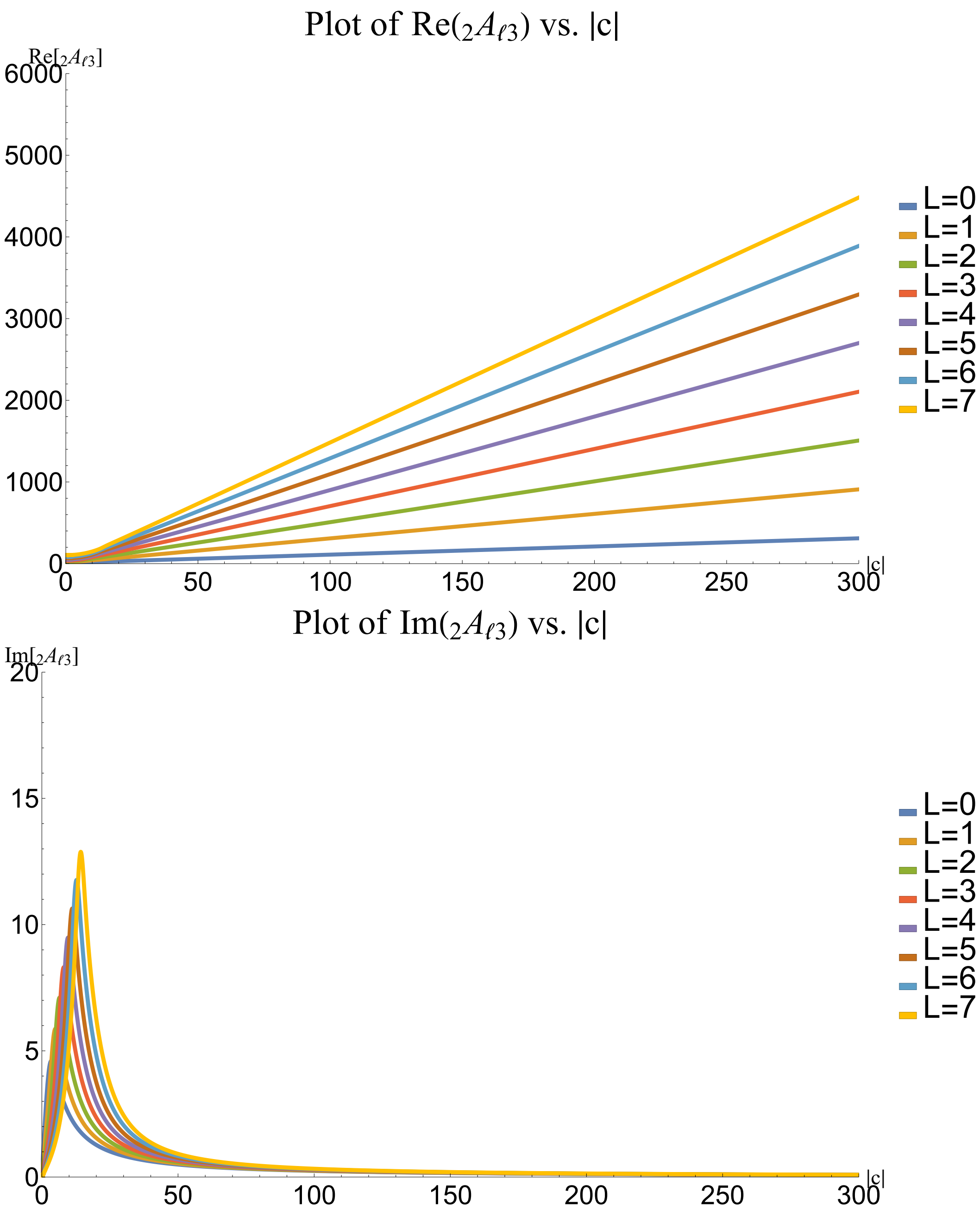

Figure 2.1: The real and imaginary components of the first 8 sequences of ${}_2A_{\ell 3}$. The plot of the real components shows linear leading order behavior, as anticipated by Eq. (1.12). The imaginary component follows a leading-order behavior of $|c|^{-1}$.

Figure 2.1 shows the behavior of the real and imaginary components of a sample collection of eigenvalue sequences, ${}_2A_{\ell 3}$. Notice that we do see the expected linear leading order behavior for the real component. A preliminary analysis showed that the real components of the eigenvalues do agree with Eq. (1.12) in this case. The imaginary component has dominant asymptotic behavior of order $|c|^{-1}$.

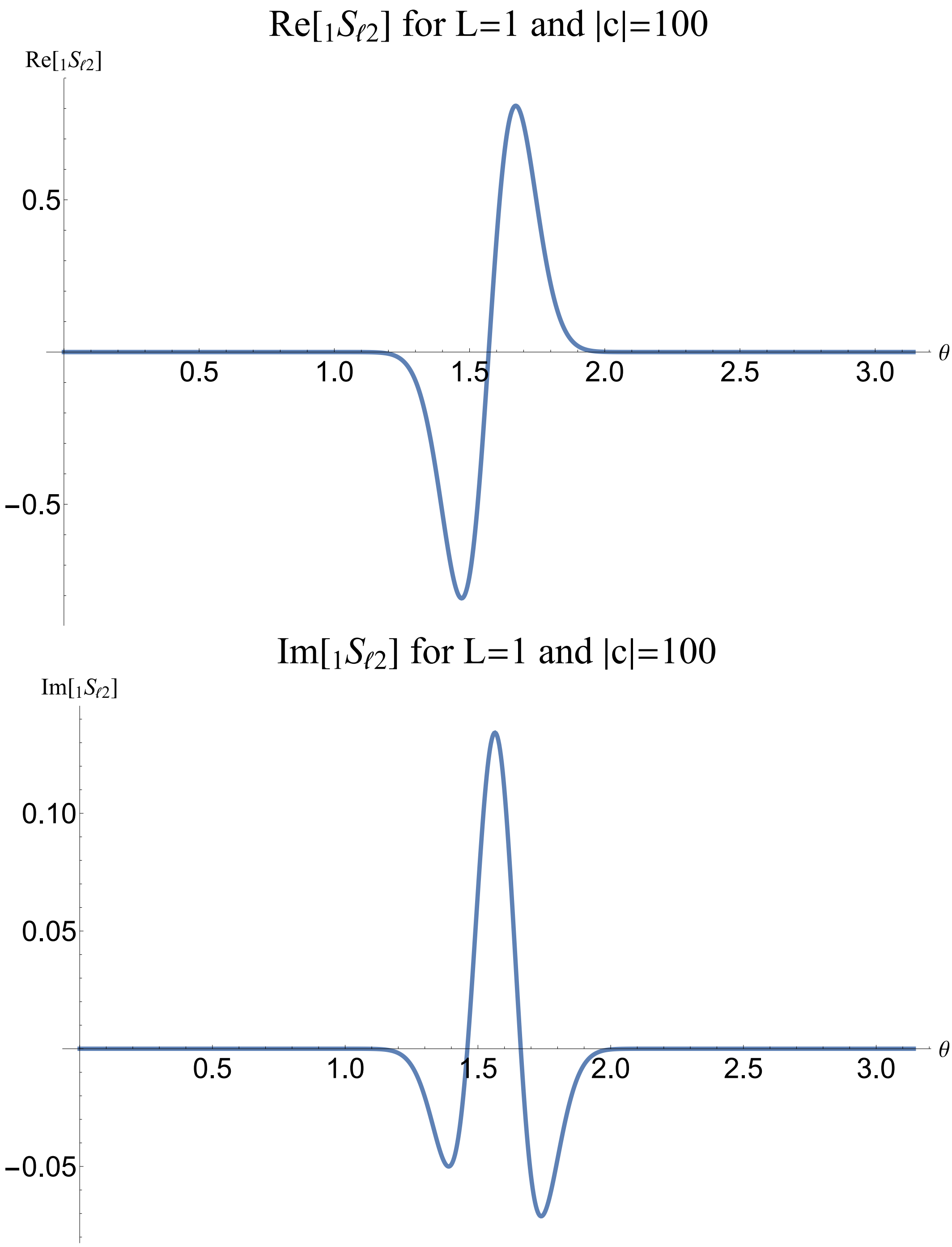

Figure 2.2: Real and imaginary components of $_1S_{32}(\theta)$ at $|c| = 100$. This plot confirms that there are $L = 1$ zero-crossings in the real components of the eigenfunction near $\theta = \pi/2$.

Figure 2.2 shows the real and imaginary components of ${}_1S_{\ell 2}$ for $L = 1$ at $ic = 100$. As can be seen, the zero-crossings of the real component do indeed occur near $\theta = \frac{\pi}{2}$, and the number of real zero-crossings in Fig. 2.2 equals L. This is representative of most of the asymptotic eigenvector solutions we found; we will discuss the exceptions to this rule later in this chapter.

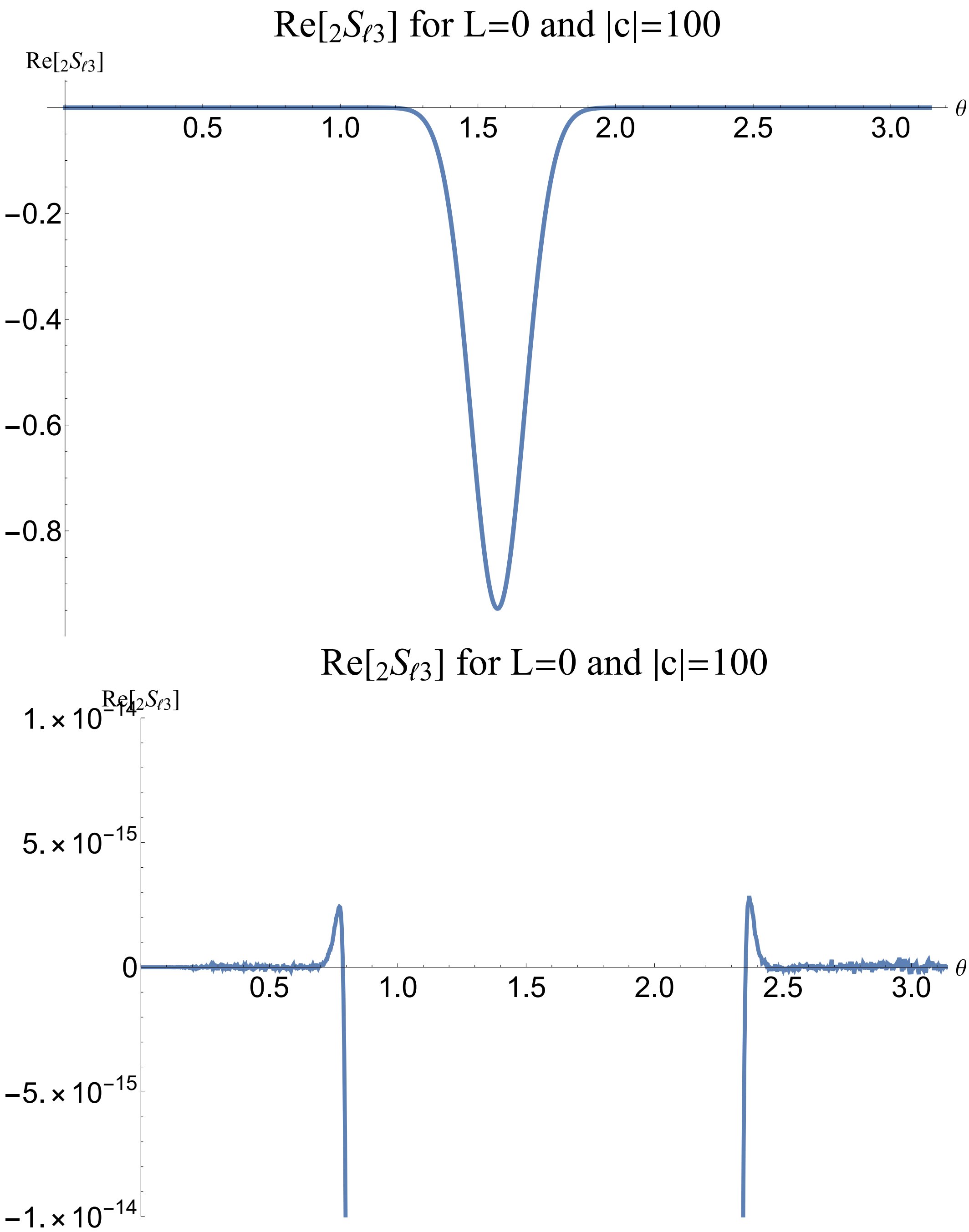

Figure 2.3: The real component of ${}_2S_{33}(\theta)$ at $|c| = 100$ with an emphasis on the real zero-crossings in the outer region. For $s = \pm 2$, one expects to see two real zero-crossings near the points of $\theta = \cos^{-1}(\pm 2^{-1/2}) \approx 0.785$ and 2.36.

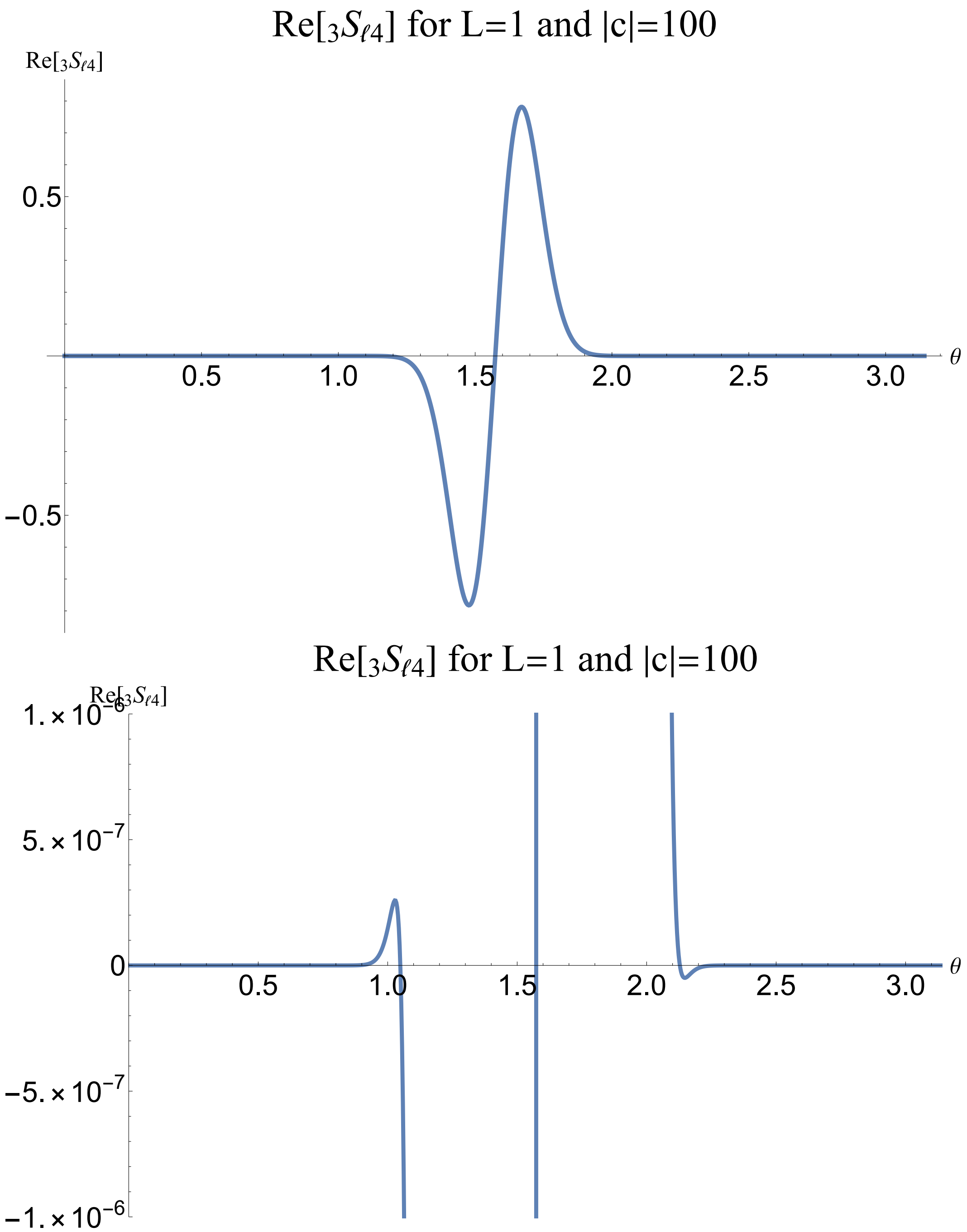

Figure 2.4: The real component of $_3S_{54}(\theta)$ at $|c| = 100$ with an emphasis on the real zero-crossings in the outer region. For $s = \pm 3$, one expects to see two real zero-crossings near the points of $\theta = \cos^{-1}(\pm 5^{-1/2}) \approx 1.11$ and 2.03.

Figure 2.2 shows no real zero-crossings in the outer region, as predicted for all $s = \pm 1$ cases by Ref. [5]. Figure 2.3 shows the real zero-crossings for ${}_2S_{\ell 3}$ for $L = 0$ at $ic = 100$. As expected for the $s = \pm 2$ cases by Ref. [5], we found two real zero-crossings near $\theta = \cos^{-1}(2^{-1/2}) \approx 0.785$ and 2.36. Figure 2.4 shows the real zero-crossings of ${}_3S_{\ell 4}$ for $L = 1$ at $ic = 100$: one crossing from the inner solution near $\frac{\pi}{2}$, and two crossings from the outer solution which were expected to be located at approximately $\theta = \cos^{-1}(\pm\frac{1}{\sqrt{5}}) \approx 1.11$ and 2.03. These crossings become less pronounced for greater magnitudes of c. For the eigenvector shown in Fig. 2.3, these crossings become indistinguishable from the numerical error around $ic \approx 110$. In general, our eigenvalue and eigenvector solutions agree with Ref. [5] in most cases. Exceptions are outlined later in this chapter.

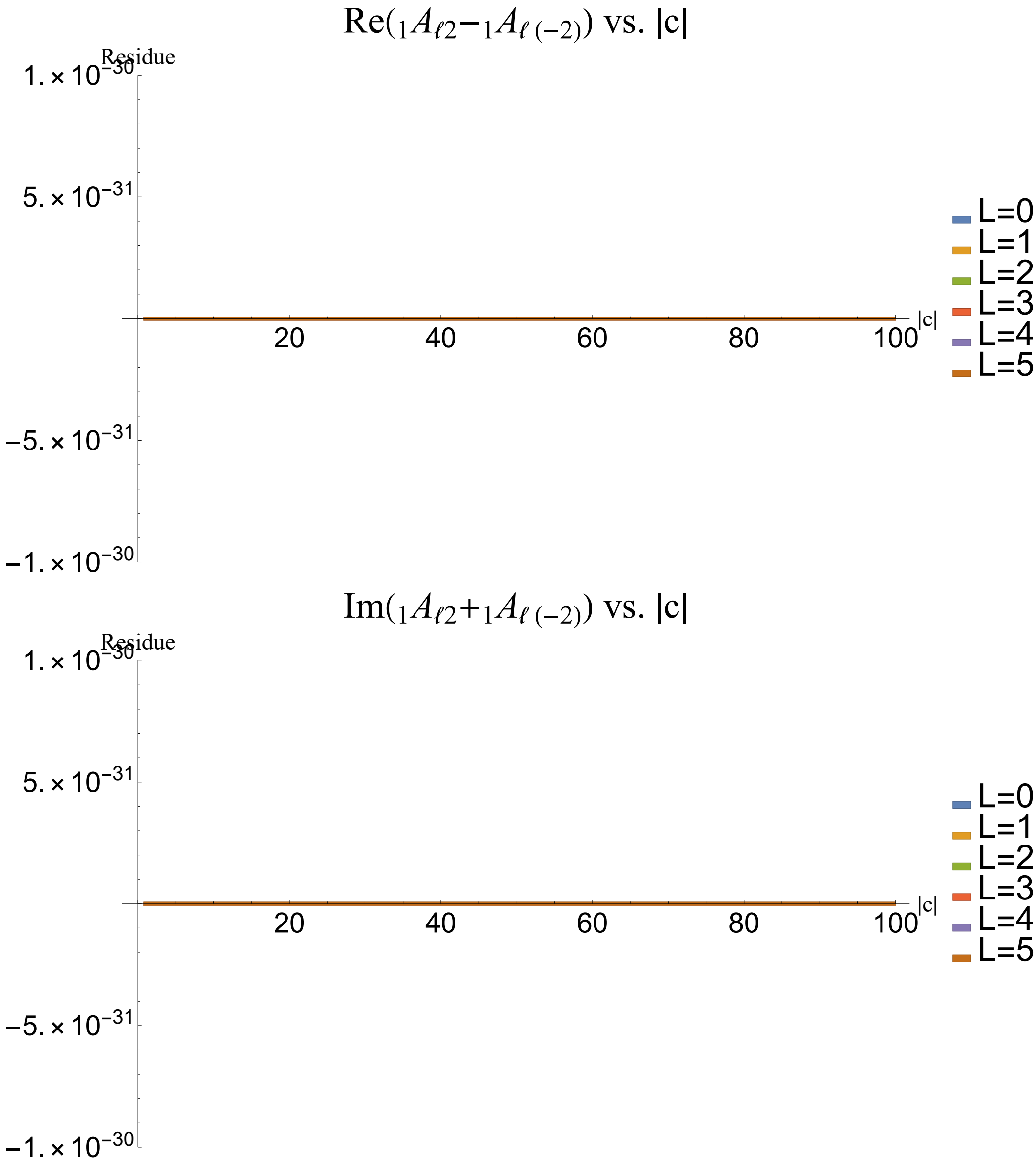

Figure 2.5: The residues of $\mathrm{Re}({}_1A_{\ell 2} - {}_1A_{\ell(-2)})$ and $\mathrm{Im}({}_1A_{\ell 2} + {}_1A_{\ell(-2)})$. Both residues are exactly zero, and this demonstrates agreement of our data with Eq. (1.1) for ${}_2A_{\ell(\pm 2)}$.

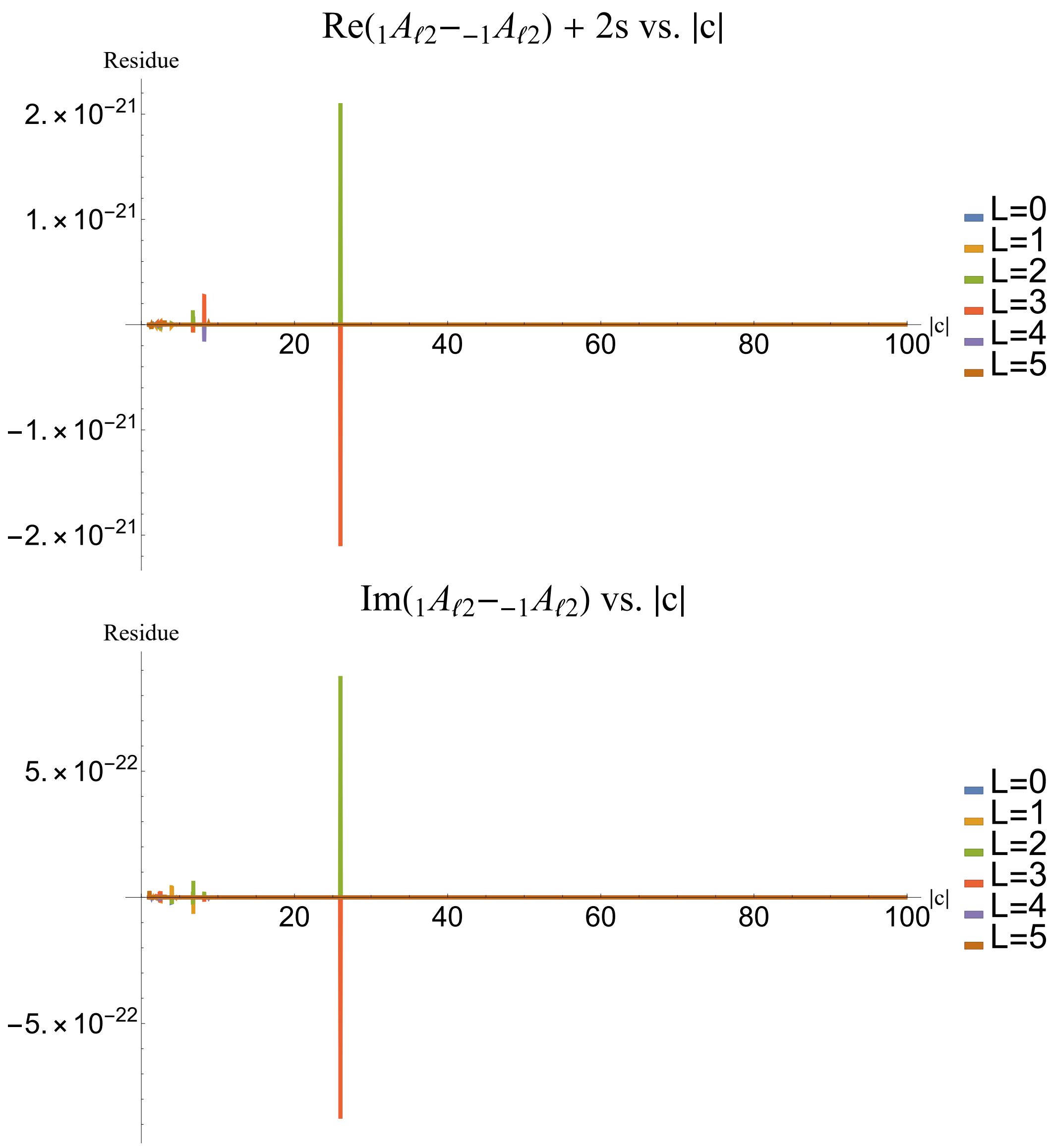

Figure 2.6: The residues of $\mathrm{Re}({}_1A_{\ell 2} - {}_{-1}A_{\ell 2}) + 2$ and $\mathrm{Im}({}_1A_{\ell 2} - {}_{-1}A_{\ell 2})$. Both residues go to zero to machine precisions, demonstrating agreement of our data with Eq. (1.2) for ${}_{\pm 2}A_{\ell 2}$.

Next, we show that our data obey the two symmetry properties of ${}_sA_{\ell m}$. Figure 2.5 is a representative plot showing the residue, or the difference, of $Re\left({}_1A_{\ell 2} - {}_1A_{\ell(-2)}\right)$ and $Im\left({}_1A_{\ell 2} + {}_1A_{\ell(-2))}\right)$. As expected, the residues are exactly zero which indicates ${}_1A_{\ell 2}$ and ${}_1A_{\ell(-2)}$ are complex conjugates of each other. This confirms that our data agrees with Eq. (1.1). Similarly, Fig. 2.6 shows $Re\left({}_1A_{\ell 2} - {}_{-1}A_{\ell 2}\right) + 2s$ and

$Im\left({}_1A_{\ell 2} - {}_{-1}A_{\ell 2)}\right)$. The residues of each go to zero out to machine precision. Figure 2.6 demonstrates agreement of our data with Eq. (1.2.) These two plots represent the symmetries for a single combination of m and s, but the behavior in Figs. 2.5 and 2.6 is demonstrative of the behavior of all eigenvalues that we generated.

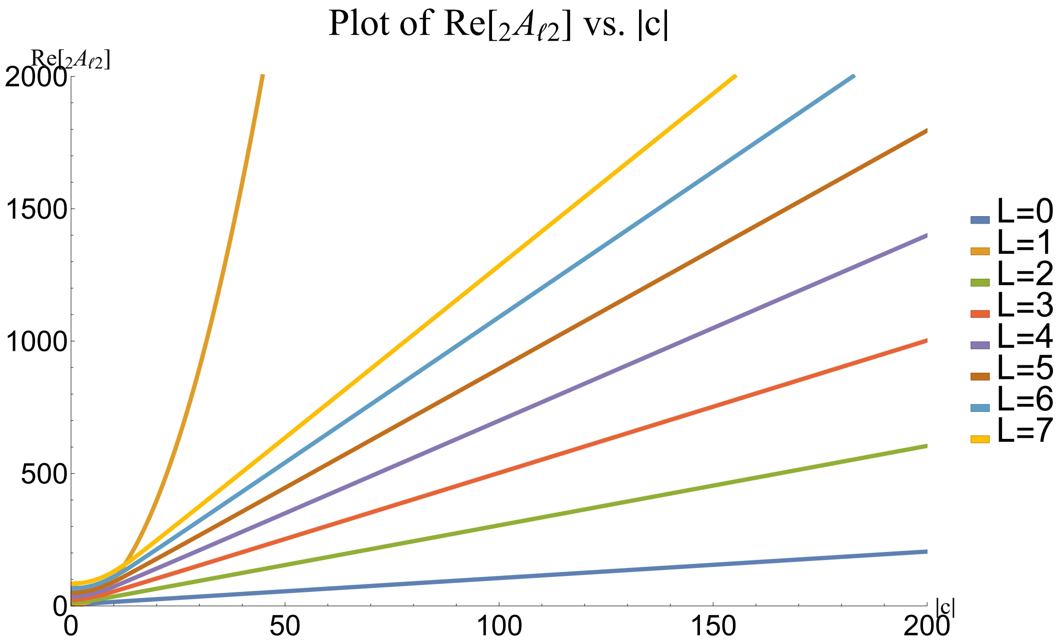

Figure 2.7: The eigenvalue sequences for Re$({}_2A_{\ell 2})$ in the asymptotic regime. Note that the $L = 1$ eigenvalue sequence has an asymptotic behavior that is quadratic which disagrees with Eq. (1.12).

It was in the observational analysis of our generated solutions that we first noticed odd behaviors in particular eigenvalue solutions, as shown in Fig. 2.7. In this figure, the eigenvalue sequence of ${}_2A_{\ell 2}$ for $L = 1$ does not exhibit linear leading order behavior, but rather quadratic behavior in the asymptotic regime.

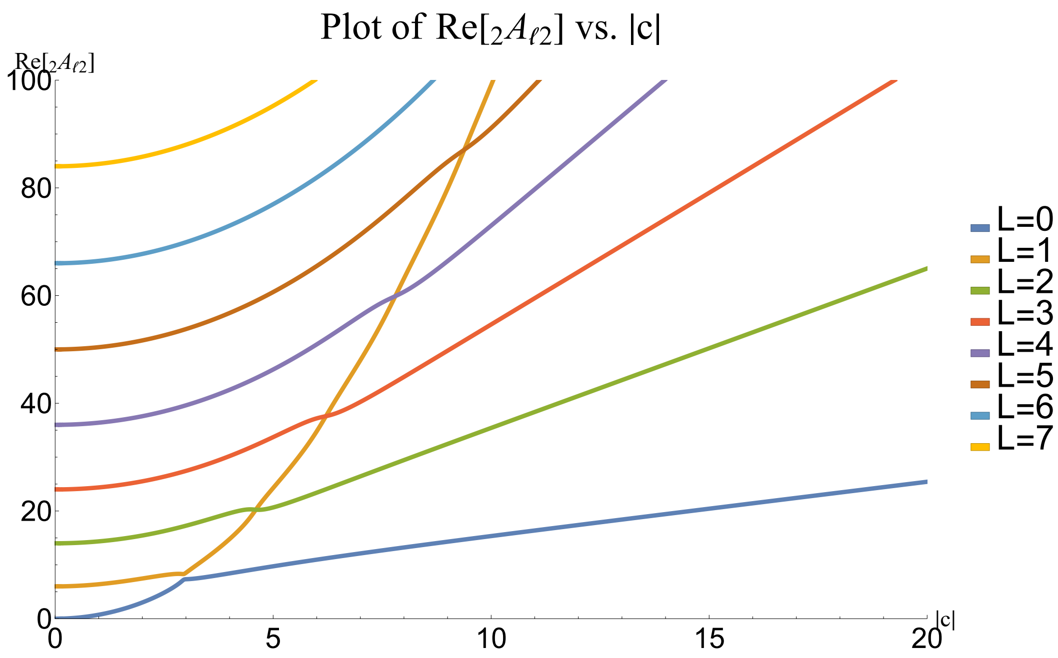

Figure 2.8: Close-up of Fig. 2.7 in the non-asymptotic regime for $\mathrm{Re}({}_2A_{\ell 2})$. Note the deflection-like event which occurs between the sequences of $L = 0$ and $L = 1$ near $ic \approx 3$. Also note the odd wobble-like behavior shown as the $L = 1$ sequence passes near the sequences of $L > 1$.

Figure 2.8 shows a close up view of the non-asymptotic regime of ${}_2A_{\ell 2}$, also shown in Fig. 2.7. Notice the deflection-like event that appears to happen between the eigenvalue sequences of $L = 0$ and $L = 1$. Sequence $L = 1$ behaves quadratically in the asymptotic regime while $L = 0$ agrees with Eq. (1.12). Berti, Cardoso, and Casals[4] also calculated the eigensolutions for $L = 0$ in this case and found the same bending behavior we did, shown in Fig. 3 of Ref. [4]. We agree with the conclusion in Ref. [4] that this bend is a smooth deformation and part of a continuous sequence.

Figure 2.8 helps to illuminate the nature of the bending behavior by showing the deflection-like event with the $L = 1$ sequence.

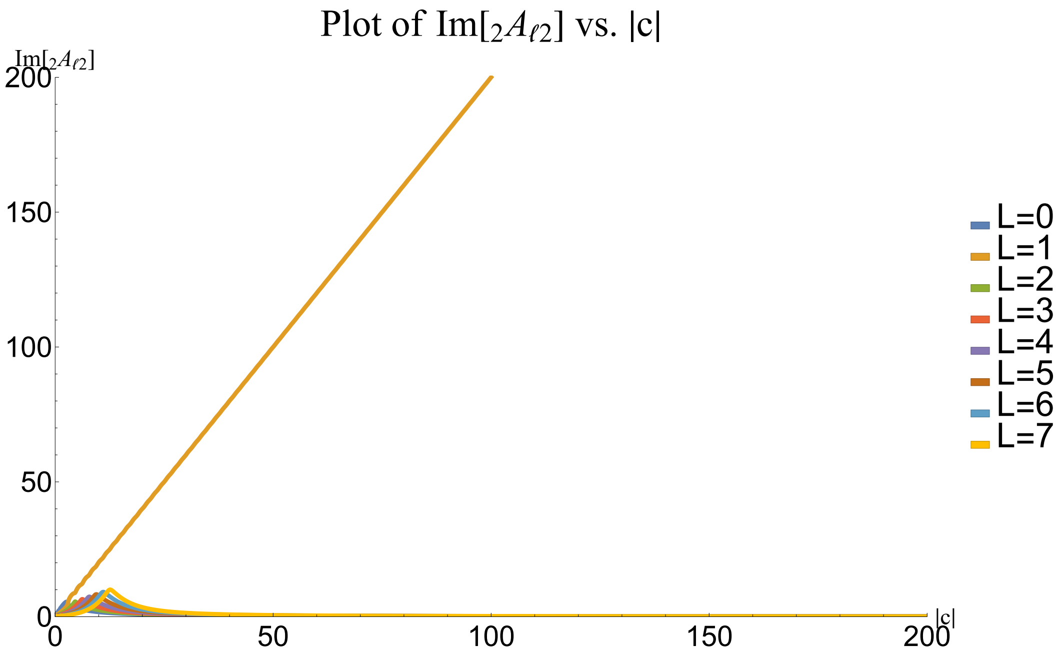

Figure 2.9: The eigenvalue sequences for $\mathrm{Im}({}_2A_{\ell 2})$ in the asymptotic regime, corresponding to the real components shown in Fig. 2.7. Note that the $L = 1$ eigenvalue sequence has an asymptotic behavior that is linear while all other sequences are of order $|c|^{-1}$.

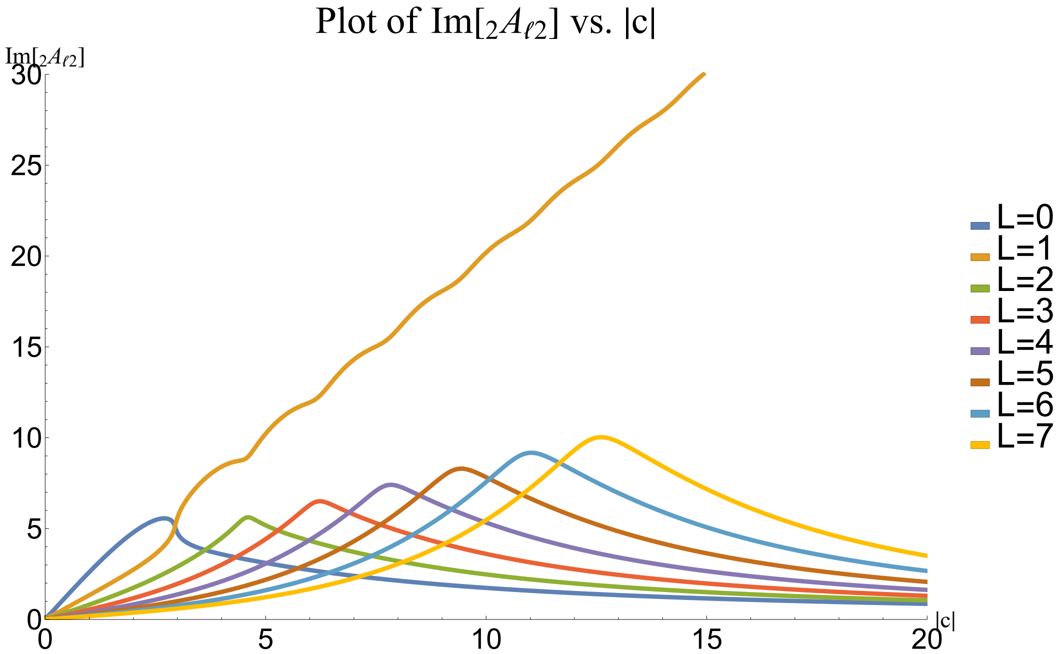

Figure 2.10: Close-up of 2.9 in the non-asymptotic regime for $\mathrm{Im}({}_2A_{\ell 2})$.Note the odd wobble-like behavior shown as the $L = 1$ sequence passes near the sequences of $L > 1$.

The behavior of the imaginary component is also different for ${}_2A_{\ell 2}$ in the case of $L = 1$. Figures 2.9 and 2.10 show the imaginary components of the same eigenvalue sequences shown in Fig. 2.7. Notice how the $L = 1$ sequence is demonstrating linear leading order behavior for the imaginary component as opposed to the $|c|^{-1}$ behavior of the other sequences. Also notice how there is a strange wobbling-like behavior each time the $L = 1$ line comes near another line. A clear example of this is near $ic \approx 5$ in Figs. 2.8 and 2.10.

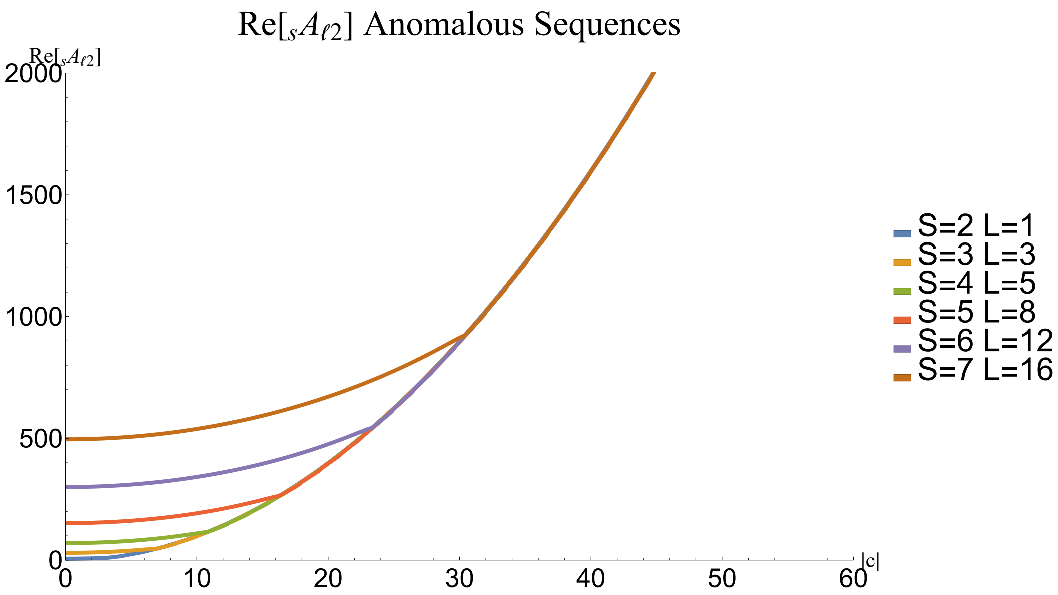

Figure 2.11: Several anomalous lines of various s and L for $m = 2$. Note that the real component of each eigenvalue sequences has quadratic asymptotic behavior, and all of these solutions may be grouped together based on this asymptotic behavior.

Other eigenvalue sequences were observed to exhibit quadratic leading order real behavior asymptotically for several combinations of m, s, and L. Each combination has a particular way of deflecting with the other sequences. We refer to these eigenvalue sequences that do not exhibit real linear leading order behavior in the asymptotic regime as "anomalous". We define an anomalous line as any prolate eigenvalue sequence which can be asymptotically fit to leading order as

$$\mathrm{Re}({}_sA_{\ell m,anom}) = |c|^2 + O(|c|^0). \tag{2.1}$$

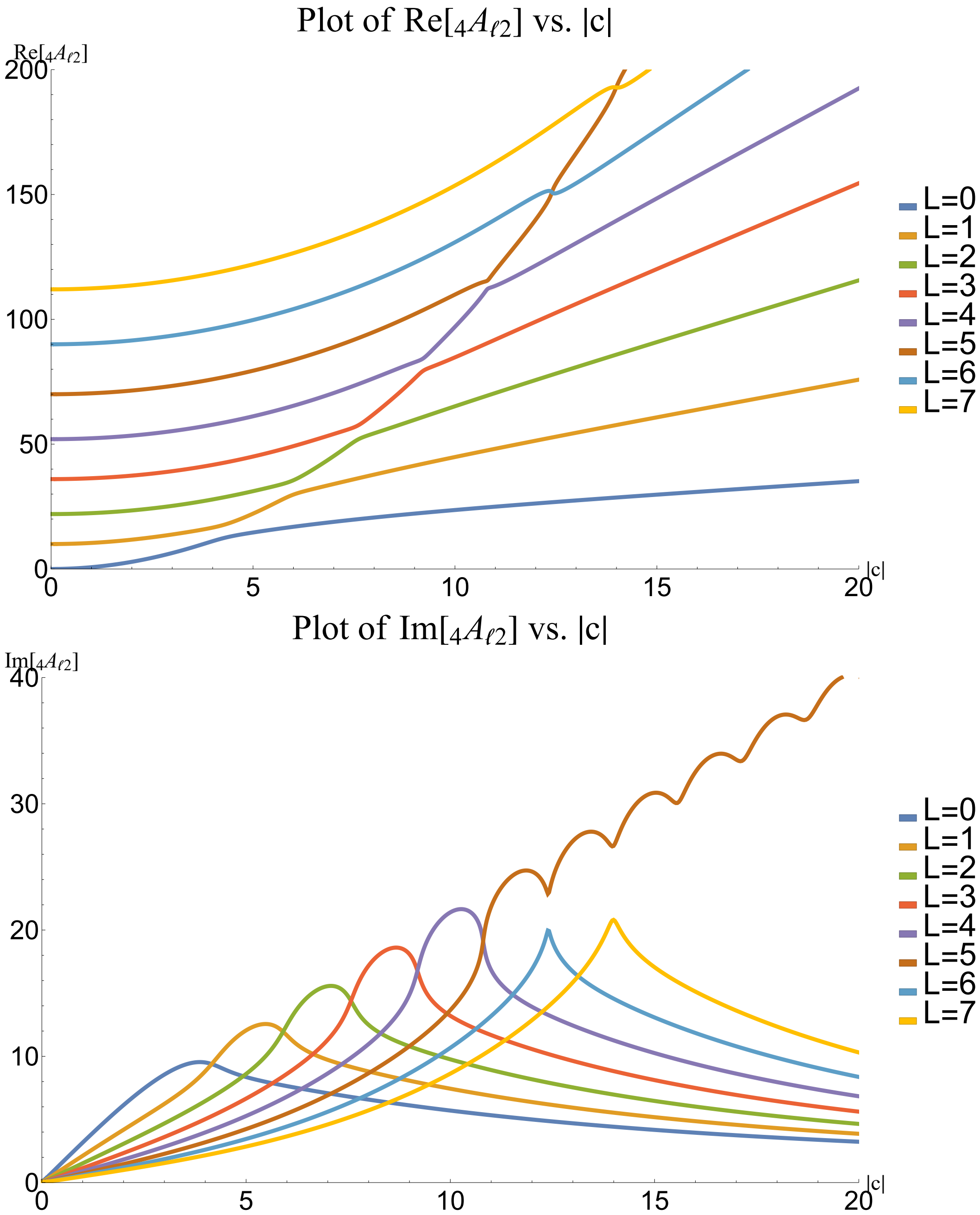

Figure 2.12: The real and imaginary components of $_4A_{\ell 2}$ in the non-asymptotic regime. Notice that the $L = 5$ eigenvalue sequence eventually demonstrates the quadratic leading-order behavior making it an anomalous eigenvalue sequence. Note the deflection-like behaviors which appear for several non-anomalous eigenvalue sequences as well as the anomalous eigenvalue sequence.

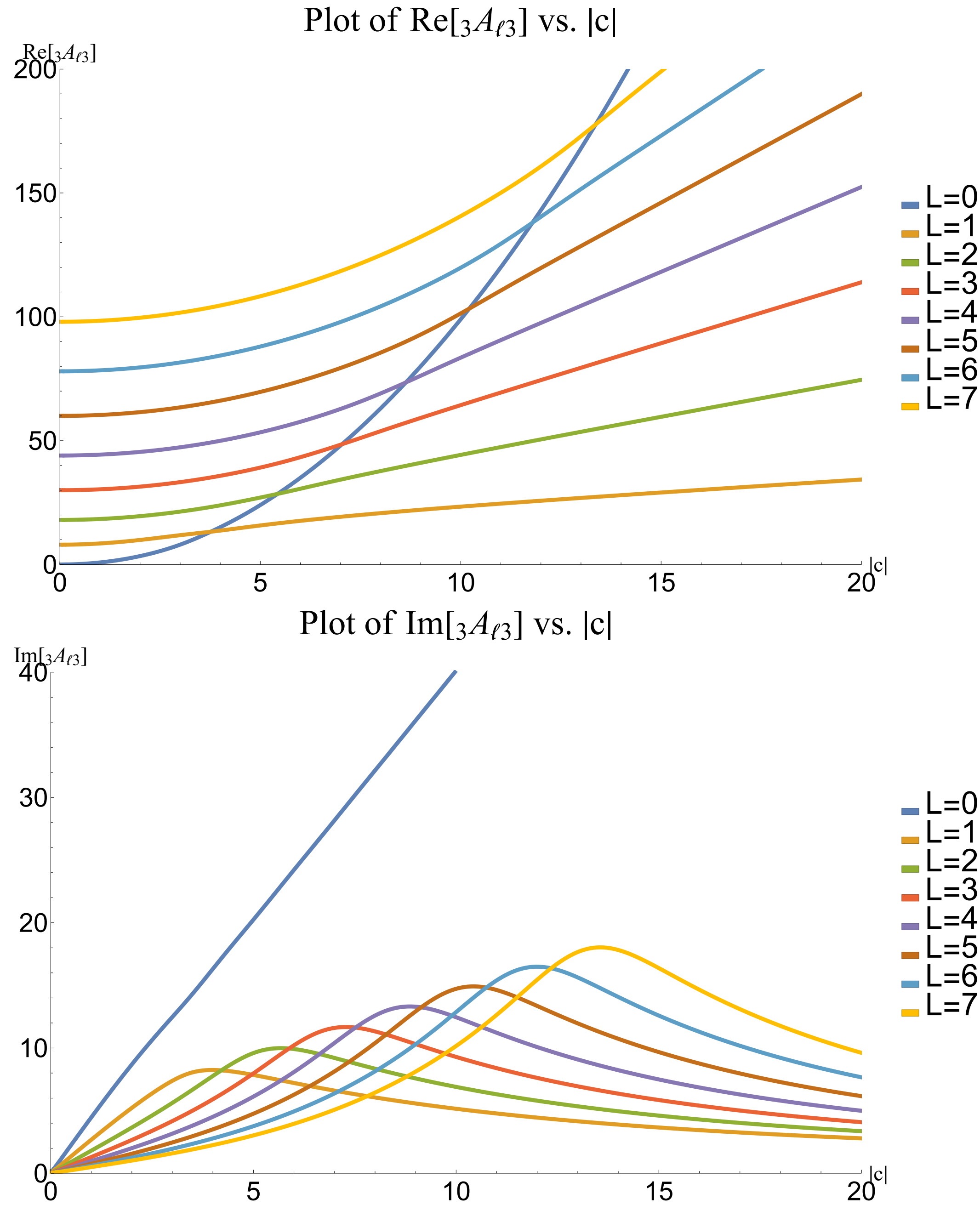

Figure 2.13: The real and imaginary components of $_3A_{\ell 3}$ in the non-asymptotic regime. Here, the $L = 0$ eigenvalue sequence is anomalous, and we note that this sequence does not exhibit any deflection-like behavior.

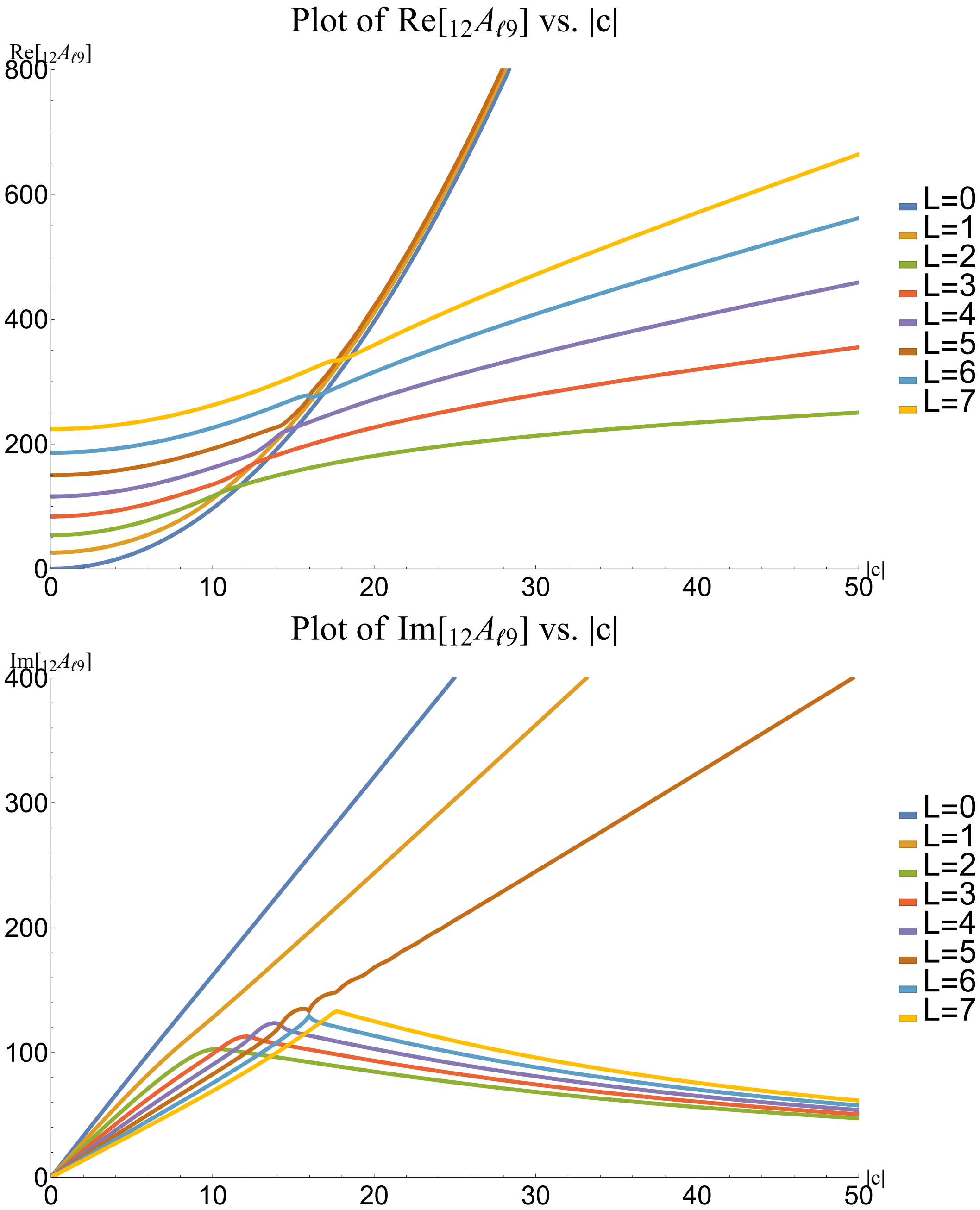

Figure 2.14: The real and imaginary components of $_{12}A_{\ell 9}$ in the non-asymptotic regime. Here, the $L = 0, 1,$ and 5 eigenvalue sequences are anomalous. There is a mixture of different deflection like behaviors present for this combination of m and s. The $L = 0$ and $L = 1$ sequences do not deflect at all while the $L = 5$ sequence does deflect.

Figure 2.12 shows that for $m = 2$ and $s = 4$ several non-anomalous eigenvalue sequences deflect off of each other until the $L = 5$ anomalous eigenvalue sequence changes to its asymptotic behavior. Figure 2.13 shows that anomalous line ${}_3A_{\ell 3}$ for $L = 0$ does not deflect at all before going on to show its asymptotic behavior. Figure 2.14 shows that for the combination of $m = 9$ and $s = 12$, there were three anomalous lines that we found—$L = 0$ and $L = 1$ did not deflect while $L = 5$ did deflect once. These plots together demonstrate the range of deflection behaviors present in the overall data.

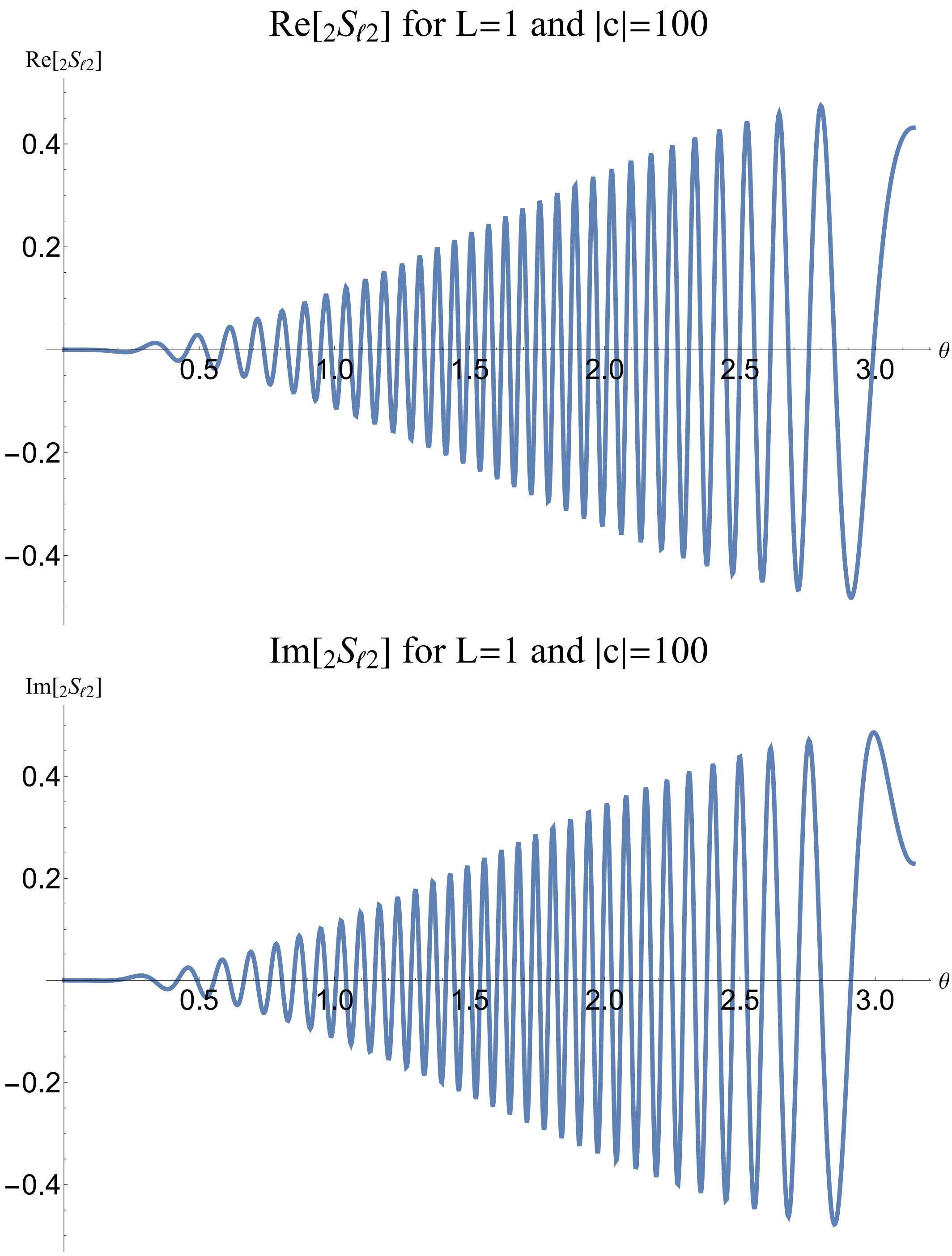

Figure 2.15: The real and imaginary components of the eigenfunction ${}_2S_{\ell 2}(\theta)$ for $L = 1$, which is an anomalous sequence. The eigenfunction is evaluated for $|c| = 100$. Notice that this sequence does not exhibit the expected behavior for the inner nor outer regions given this combination of L and s. Also note that this eigenfunction does not go to zero at both endpoints.

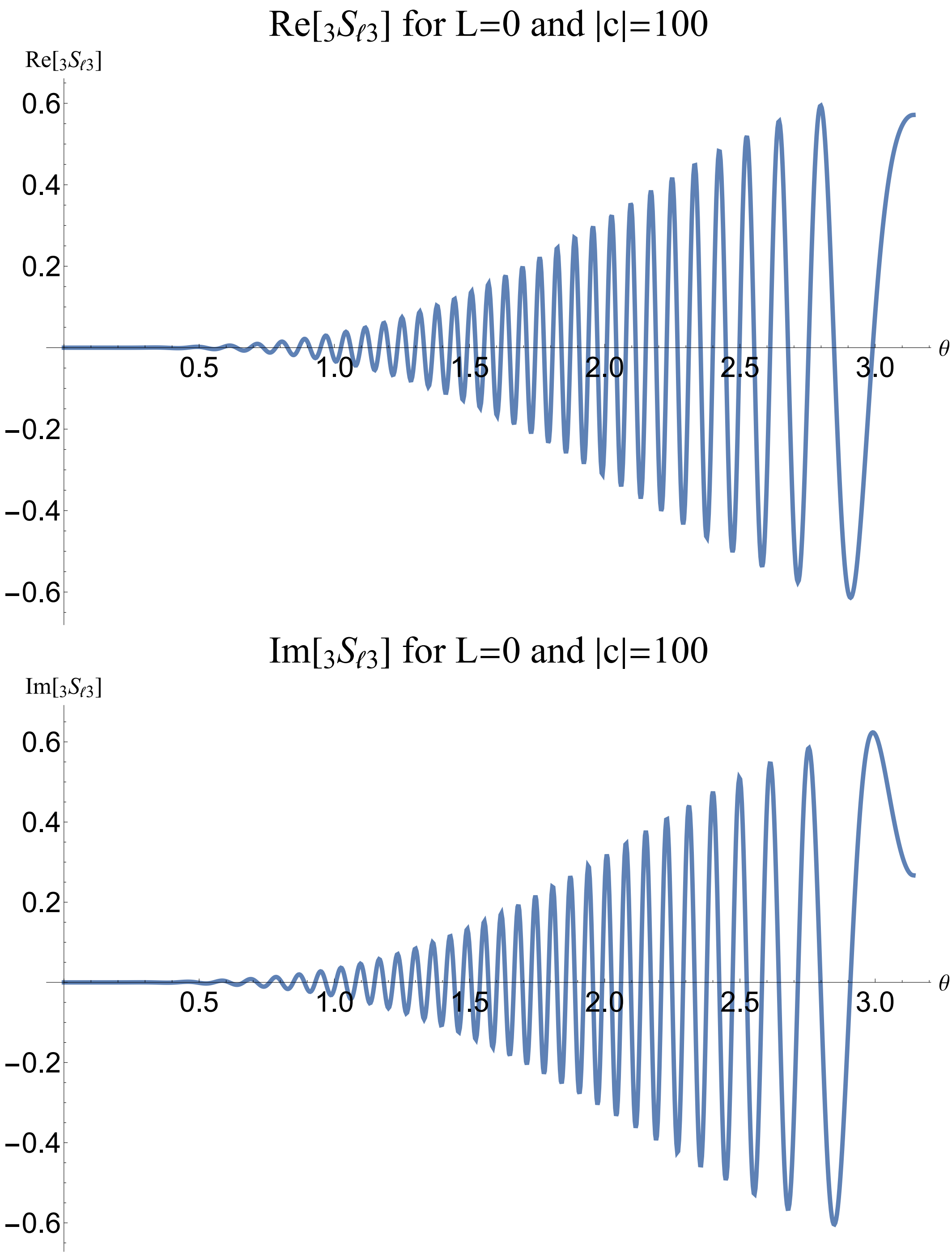

Figure 2.16: The real and imaginary components of the eigenfunction ${}_3S_{\ell 3}(\theta)$ for $L = 0$, which is an anomalous sequence. The eigenfunction is evaluated for $|c| = 100$. Notice that this sequence does not exhibit the expected behavior for the inner nor outer regions given this combination of L and s. Also note that this eigenfunction does not go to zero at both endpoints.

Figures 2.15 and 2.16 are eigenvector solutions for ${}_2S_{\ell 2}$ for $L = 1$ and ${}_3S_{\ell 3}$ for $L = 0$ respectively at $ic = 100$ and both are anomalous. As can be seen in both figures, these anomalous lines do not have a number of real zero-crossings which agree with the inner and outer solutions outlined in Ref. [5] and Ref. [4]. For anomalous lines, the number of zero-crossings increases approximately linearly with $|c|$ in the asymptotic regime so that they do not approach any fixed number of real zero-crossings. Also note how the anomalous eigenvectors do not go to zero at the endpoints, which was an assumption in the derivation of Eq. (1.12). While there are anomalous eigenvalue sequences which do go to zero at the end points, this assumption may partially account for why the anomalous eigenvalue sequences have not been previously predicted.

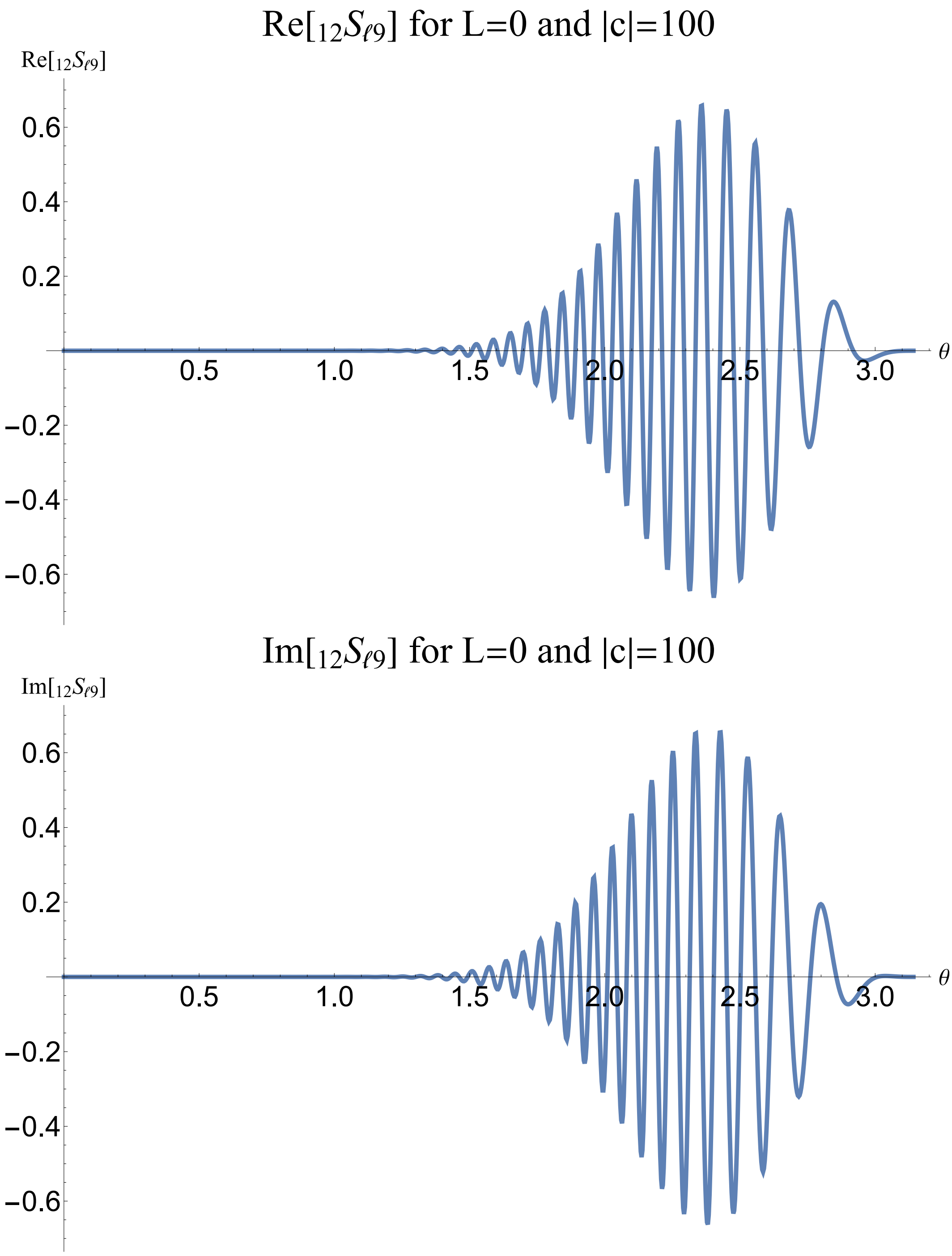

Figure 2.17: The real and imaginary components of the eigenfunction $_{12}S_{\ell 9}(\theta)$ for $L = 0$, which is an anomalous sequence. The eigenfunction is evaluated for $|c| = 100$. Note that this anomalous eigenvector solution does go to zero at both endpoints.

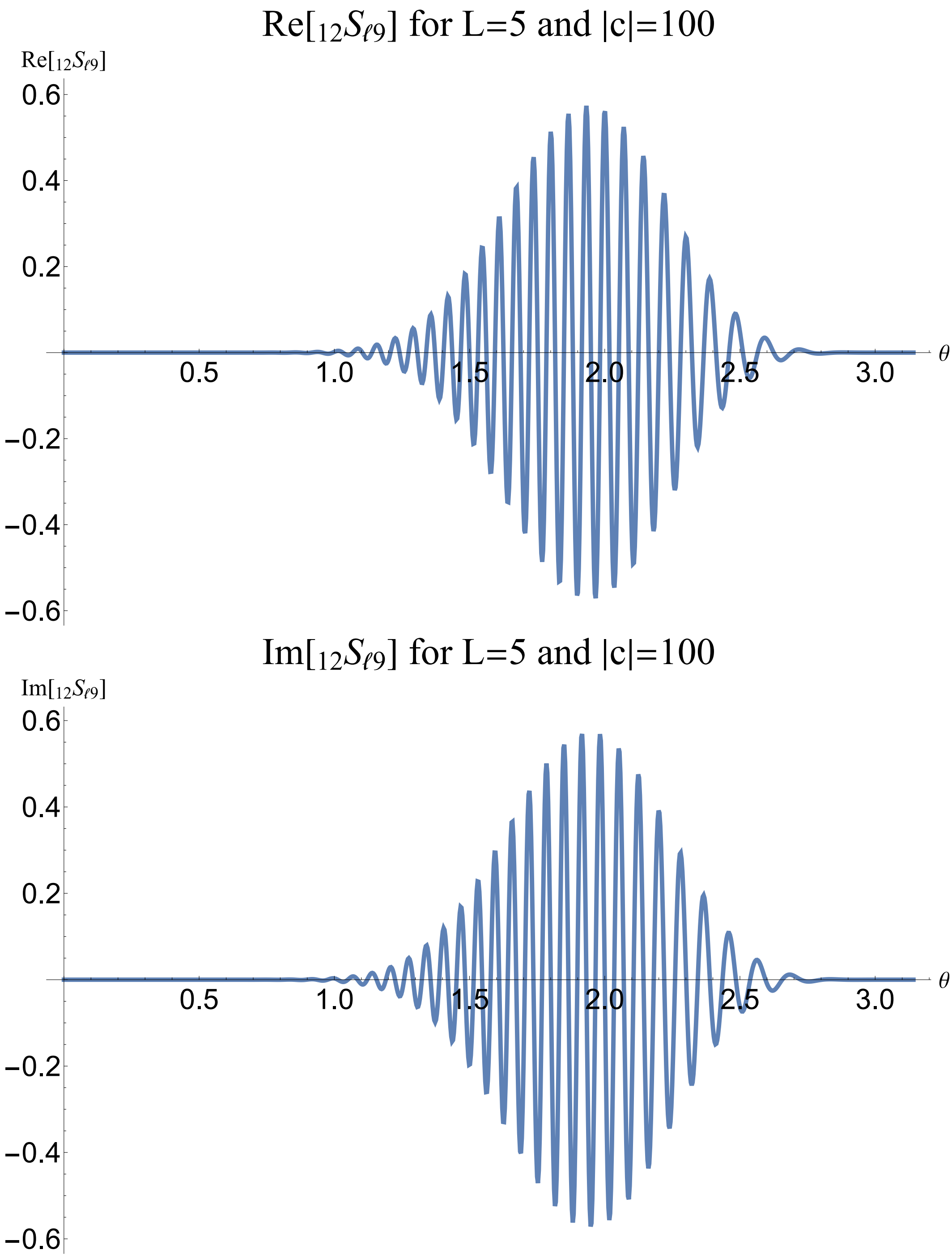

Figure 2.18: The real and imaginary components of the eigenfunction ${}_{12}S_{\ell 9}(\theta)$ for $L = 5$, which is an anomalous sequence. The eigenfunction is evaluated for $|c| = 100$.

Figures 2.17 and 2.18 show how having real zero-crossings near the endpoints is not consistent across all anomalous eigenvector lines.

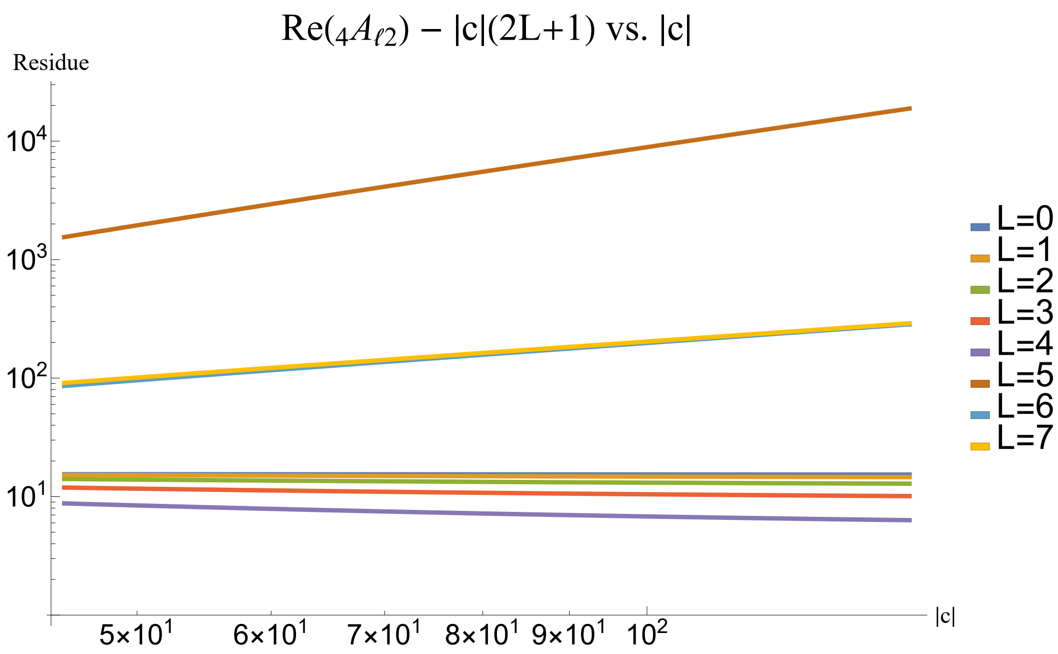

Figure 2.19: Log-log plot of the residue for Re($_{-4}A_{\ell 2}$) after subtracting the leading-order analytic asymptotic behavior given in Eq. (1.12). The eigenvalue sequence of $L = 5$ is anomalous. This plot shows three distinct categories of sequences. The sequences with $L < 5$ are of constant order in $|c|$, which agrees with Eq. (1.12). The $L = 5$ residue is of order $|c|^2$, which is expected for any anomalous eigenvalue sequence. Note the residues for $L > 5$ are of linear order in $|c|$. This indicates that the asymptotic behavior of these sequences is still linear in $|c|$ but does not agree with the leading-order analytic asymptotic behavior given in Eq. (1.12).

Other odd behaviors appear for the non-anomalous lines that share a combination of m and s with at least one anomalous line. For an anomalous line present at $L = l$, it turns out that the eigenvalue sequences of $L > l$ still show linear leading-order real behavior but do not agree with Eq. (1.12). This interaction is best demonstrated in Fig. 2.19. For a non-anomalous line, we expect the residue of ${}_sA_{\ell m} - |c|(2L+1) = O(|c|^0)$, which would correlate to a flat line in the log-log plot. The $L = 5$ eigenvalue sequence is the anomalous line for $m = 2$ $s = 4$ shown in Fig. 2.19. For eigenvalues of $L < 5$, the leading order behaviors of the residues are constant. For $L > 5$, the residues show linear leading order behavior, in disagreement with Eq. (1.12).

Not obvious in Fig. 2.19, the eigenvalue sequence of $L = 6$ actually has a leading order behavior $\lim_{ic\to\infty} {}_4A_{10,2} = 11|c|$ which is the expected behavior for $L = 5$. Likewise, $L = 7$ exhibits the expected behavior of the $L = 6$ sequence and so on for all higher values of L for this combination of m and s.

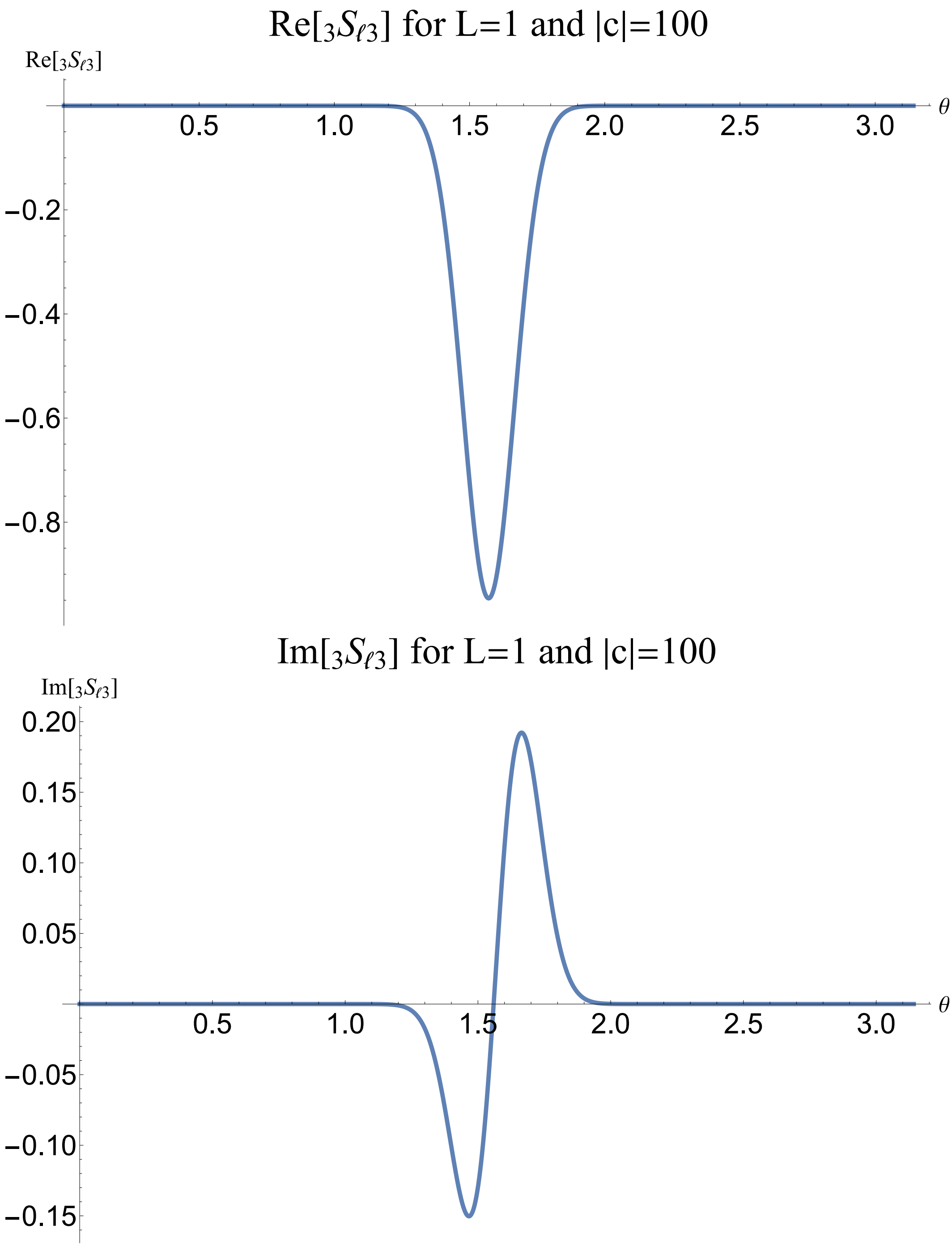

Figure 2.20: The real and imaginary components of the non-anomalous eigenfunction ${}_3S_{\ell 3}(\theta)$ with $L = 1$ at $ic = 100$. Based on the predictions from Ref. [4], one would expect one zero-crossing of the real component in the inner region since $L = 1$. Note that there are no real zero-crossings in the inner region; one less than expected. Recall that the corresponding $L = 0$ sequence is anomalous.

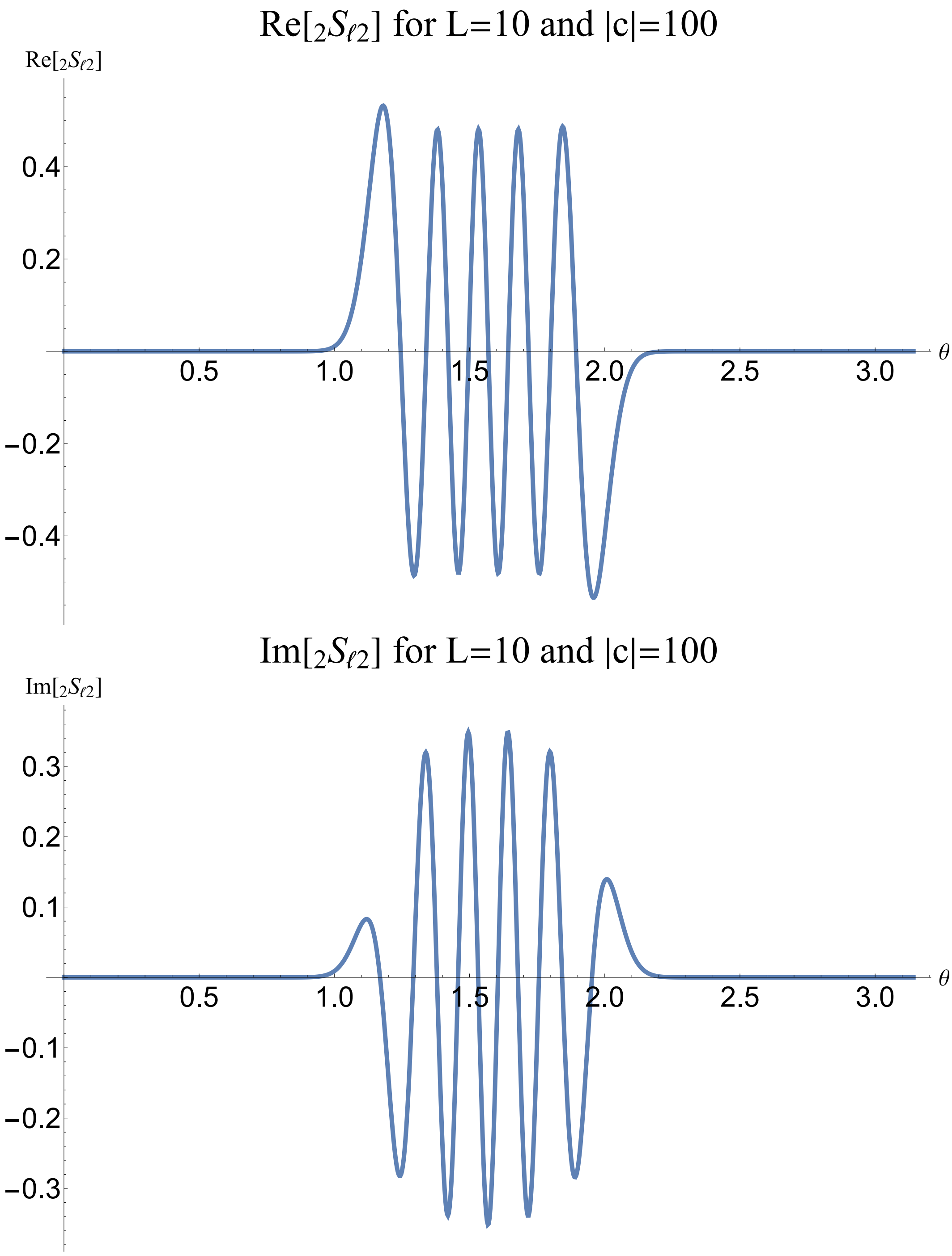

Figure 2.21: The real and imaginary components of the non-anomalous eigenfunction $_2S_{\ell 2}(\theta)$ for $L = 10$ at $ic = 100$. Based on the predictions from Ref. [4], one would expect $L = 10$ zero-crossing of the real component in the inner region. Note that there are nine real zero-crossings of the inner region; one less than expected. Recall that the corresponding $L = 1$ sequence is anomalous. Along with Fig. 2.20, this demonstrates a shift in the observed eigenfunction zero-crossings due to the existence of anomalous sequences of same m and s.

Figures 2.20 and 2.21 show the non-anomalous eigenvector solutions for the asymptotic cases of ${}_3S_{\ell 3}$ for $L = 1$ and ${}_2S_{\ell 2}$ for $L = 10$ at $ic = 100$. Recall from Fig. 2.13 that $L = 0$ of ${}_3S_{\ell 3}$ is an anomalous eigenvalue line. $L = 1$ of ${}_3S_{\ell 3}$ is expected to have one real eigenvector zero-crossing, but notice the number of zero-crossings is actually 0. Similarly for ${}_2S_{\ell 2}$, $L = 1$ is anomalous, and the number of real zero-crossings of $L = 10$ is one less than expected. In all cases, the number of real zero-crossings appears to be less than expected in the asymptotic limit due to the presence of anomalous eigenvector solutions of lower L.

L is merely an arbitrary label assigned based on an eigenvalue's behavior in the spherical limit. The shifting behaviors noted above show that it would be useful to assign a new index other than L in the asymptotic limit. This lead us to define $L' = L - {}_sN_{\ell m}$. ${}_sN_{\ell m}$ is the number of anomalous eigenvalues such that for $l < \ell$, ${}_sA_{lm}$ is anomalous. It is then true that for all non-anomalous eigenvalue sequences,

$$ {}_sA_{\ell m} = |c|\left(2L' + 1\right) + O\left(|c|^0\right). \tag{2.2}$$

It is also true that the number of real zero-crossings for non-anomalous eigenvectors in the inner region is equal to L'.

It is very clear that we will have to separately fit the anomalous and non-anomalous eigenvalue sequences. We will first fit the non-anomalous solutions as those will most-closely resemble the $s = 0$ solutions and Eq. (1.12). We will then explore the fits for the anomalous eigenvalue sequences.

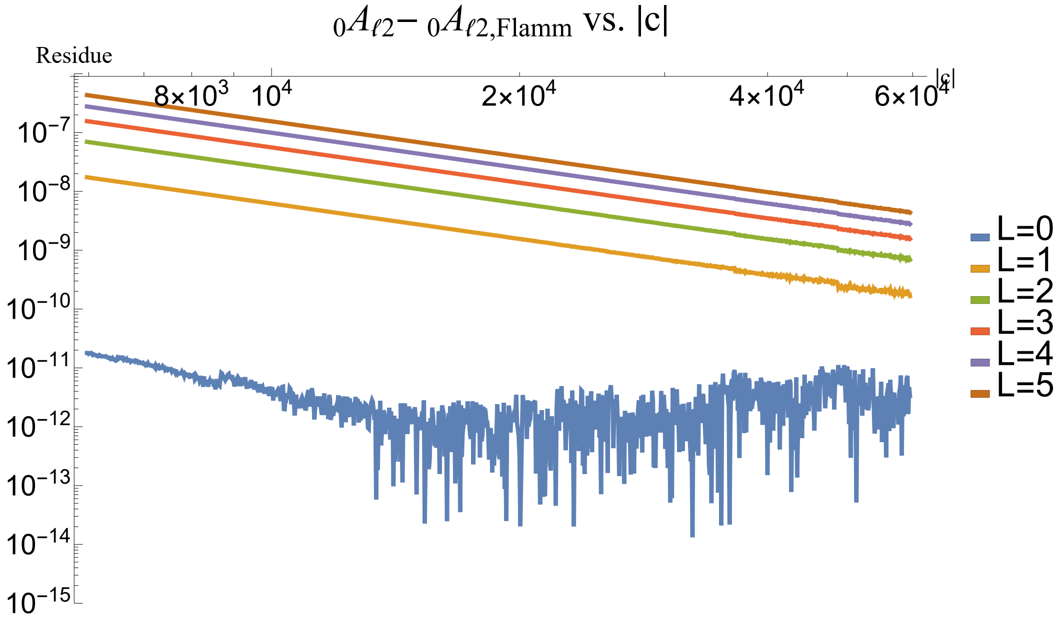

Figure 3.1: Residues of our numerical solutions for ${}_0A_{\ell 2}$ minus the analytic expectation of Eq. (1.10) truncated at order $|c|^{-2}$. The residue of the $L = 0$ sequence reaches machine precision while the residues for $L > 0$ are of order $|c|^{-2}$.

Before exploring the fitting of ${}_sA_{\ell m}$ for $|s| > 0$, we first wanted to confirm our numerical results with the known analytic solution for ${}_0A_{\ell m}$, which Flammer[15] derived and we display in Eq. (1.10). Figure 3.1 shows the residue of subtracting Eq. (1.10) truncated at order $|c|^{-2}$ from our numerical results for ${}_0A_{\ell 2}$. The $L = 0$ residue reached machine precision while the $L > 0$ residues had slopes of -2 in the log-log plot, indicating a remaining residue of order $|c|^{-2}$. This shows a disagreement between our numerical data and Eq. (1.10). A preliminary analysis of this residue behavior appears to go as ${}_0A_{\ell m} - {}_0A_{\ell m,Flamm} = -\frac{40L^2}{64|c|^2} + O(|c|^{-3})$.

At this point, we chose to analytically check Flammer's original solution from Ref. [15] to ensure the accuracy of our numerical results. Starting with the Eq. (0.3) for $s = 0$, Flammer makes the substitution

$$ {}_0S_{\ell m} = \left(1 - \eta^2\right)^{1/2} u_{\ell m}, \tag{3.1} $$

where $\eta = 2|c|^{-1/2}x$. This substitution yields

$$ \left(2|c| - x^2\right) \frac{d^2u_{\ell m}}{dx^2} - 2\left(m+1\right) x \frac{du_{\ell m}}{dx} + \left[{}_0A_{\ell m} - m^2 - m - \frac{1}{2}|c|x^2 \right] u_{\ell m} = 0. \tag{3.2} $$

In the asymptotic limit, $|c| \gg x$ and Eq. (3.2) reduces to

$$ \frac{d^2u_{\ell m}}{dx^2} + \left(\frac{1}{2|c|} \, {}_0A_{\ell m} - \frac{1}{4}x^2 \right) u_{\ell m} = 0. \tag{3.3} $$

Equation (3.3) is a differential equation with a similar form to the equation defining the parabolic cylinder functions D_r, shown in Eq. (1.9). Thus, the number of zero-crossings in this limit are determined by the parabolic cylinder functions, which have

r zero crossings.

For $c = 0$, Eq. (0.3) reduces to the differential equation for ${}_sY_{\ell m}$, which has $\ell - |m|$ zero crossings. Flammer notes that the number of zero-crossings of ${}_0S_{\ell m}$ must remain the same for all values of c. With this, he was able to use Eqs. (3.3) and (1.9) to conclude in the asymptotic limit ${}_0A_{\ell m} = (2r+1)|c|$ and therefore

$$\lim_{c \to \pm i\infty} {}_0A_{\ell m} = |c|\,(2\ell - 2|m| + 1) = |c|\,(2L+1)\,. \tag{3.4}$$

Flammer then expands $u_{\ell m}$ in terms of the parabolic cylinder functions so

$$u_{\ell m} = \sum_{r=-\infty}^{\infty} h_r^L D_{L+r}. \tag{3.5}$$

Plugging Eq. (3.5) into Eq. (3.2) for even r, Flammer derives the recursion relation

$$\begin{aligned} 0 = &- h_{r-4}^L + 4m h_{r-2}^L + \left[4\,{}_0A_{\ell m} - 8c\left(L + r + \frac{1}{2}\right) - 4m^2 + \right. \\ &\left. 2(L+r)^2 + 2(L+r) + 3\right] h_r^L - 4m(L+r+1)(L+r+2)h_{r+2}^L - \\ &(L+r+1)(L+r+2)(L+r+3)(L+r+4)h_{r+4}^L. \end{aligned} \tag{3.6}$$

We used Eqs. (3.4) and (3.6) to solve for h_r^L by the method of successive approximation after noting that

$$h^L_{\pm(2r+2)}/h^L_0 = O(|c|^{-\frac{1}{2}r-1}), \text{ and } h^L_{\pm(2r+4)}/h^L_0 = O(|c|^{-\frac{1}{2}r-1}). \tag{3.7}$$

There are a countably infinite number of h^L_r functions each with a countably infinite number of terms. We only solved the functions needed to a depth necessary to reproduce the result from Ref. [15] for Eq. (1.10) out to order $|c|^{-2}$. Our solutions for the values of h_r^L were consistent with those found by Flammer, and are

$$
\begin{aligned}
\frac{h_2^L}{h_0^L} =& 2^{-2}m\Bigg(|c|^{-1} - \left(L^2-25L-36\right)2^{-5}|c|^{-2} \\
&- \left[6L^3-99L^2-275L-252+4m^2\left(L^2-L+8\right)\right]2^{-7}|c|^{-3}\Bigg) + O\left(|c|^{-4}\right), \\
\frac{h_{-2}^L}{h_0^L} =& 2^{-2}m\Bigg(|c|^{-1} + \left(L^2+27L-10\right)2^{-5}|c|^{-2} \\
&+ \left[6L^3+117L^2-59L+82-4m^2\left(L^2+3L+10\right)\right]2^{-7}|c|^{-3}\Bigg)\frac{L!}{(L-2)!} \\
&+ O\left(|c|^{-4}\right), \\
\frac{h_4^L}{h_0^L} =& -2^{-5}\Bigg(|c|^{-1} + \left(2L+5-4m^2\right)2^{-2}|c|^{-2} + \Big[(L+5)(L+6)(L+7)(L+8)2^{-7} \\
&- \left(2L^3-29L^2-153L-197\right)2^{-3} - m^2\left(24L+52\right)\Big]2^{-4}|c|^{-3}\Bigg) + O\left(|c|^{-4}\right), \\
\frac{h_{-4}^L}{h_0^L} =& 2^{-5}\Bigg(|c|^{-1} + \left(2L-3+4m^2\right)2^{-2}|c|^{-2} + \Big[(L-4)(L-5)(L-6)(L-7)2^{-7} \\
&+ \left(2L^3+35L^2-89L+75\right)2^{-3} + m^2(24L-28)\Big]2^{-4}|c|^{-3}\Bigg)\frac{L!}{(L-4)!} \\
&+ O\left(|c|^{-4}\right), \\
\frac{h_6^L}{h_0^L} =& -2^{-7}m\left[|c|^{-2} - \left(3L^2-243L-616+64m^2\right)3^{-1}2^{-6}|c|^{-3}\right] + O\left(|c|^{-4}\right), \\
\frac{h_{-6}^L}{h_0^L} =& 2^{-7}m\left[|c|^{-2} + \left(3L^2+249L-370+64m^2\right)3^{-1}2^{-6}|c|^{-3}\right]\frac{L!}{(L-6)!} + O\left(|c|^{-4}\right), \\
\frac{h_8^L}{h_0^L} =& 2^{-11}\left[|c|^{-2} + \left(2L+7-4m^2\right)2^{-1}|c|^{-3}\right] + O\left(|c|^{-4}\right), \\
\frac{h_{-8}^L}{h_0^L} =& 2^{-11}\left[|c|^{-2} + \left(2L-5+4m^2\right)2^{-1}|c|^{-3}\right]\frac{L!}{(L-8)!} + O\left(|c|^{-4}\right),
\end{aligned}
\tag{3.8}
$$

When plugging these values of h_r^L into Eq. (3.6), we arrived at the solution

$$
\begin{aligned}
{}_0A_{\ell m,analytic} =& |c|\,(2L+1) - \left(2L^2+2L+3-4m^2\right)2^{-2} \\
& - \frac{1}{|c|}\,(2L+1)\left(L^2+L+3-8m^2\right)2^{-4} \\
& - \frac{1}{|c|^2}\left[5\left(L^4+2L^3+8L^2+7L+3\right) - 48m^2\left(2L^2+2L+1\right)\right]2^{-6} \\
& + O\left(|c|^{-3}\right).
\end{aligned} \tag{3.9}
$$

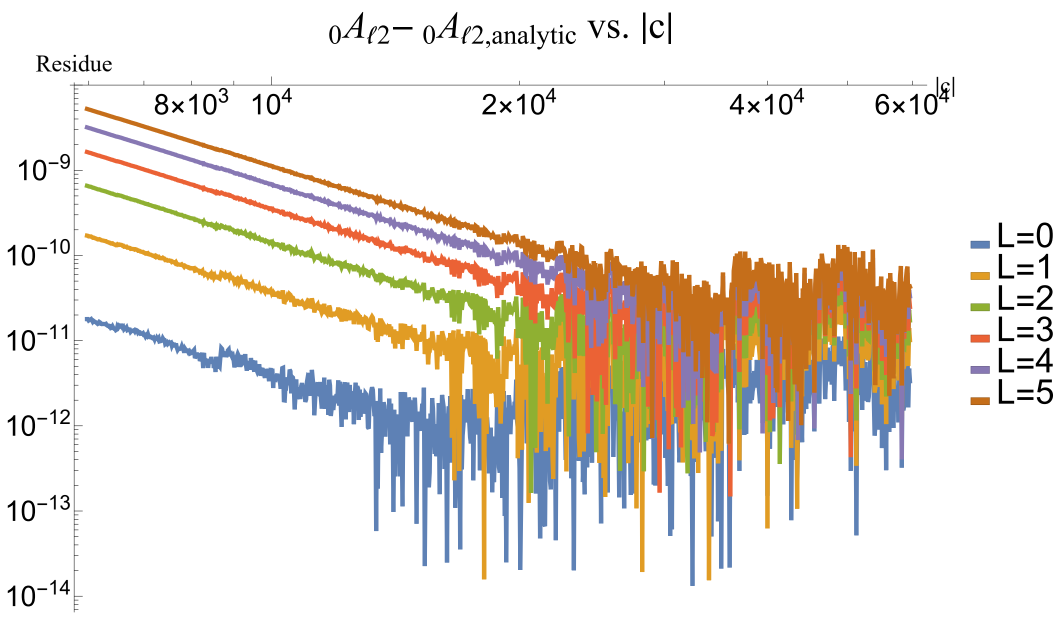

Figure 3.2: Residues of our numerical solutions for ${}_0A_{\ell 2}$ minus the analytic expectation of Eq. (3.9) truncated at order $|c|^{-2}$. The residue of all sequences reach machine precision, indicating that the analytic correction made in Eq. (3.9) is in agreement with our numerical data.

When subtracting Eq. (1.10) from our analytic solution, we found that ${}_0A_{\ell m,analytic} - {}_0A_{\ell m,Flamm} = -\frac{40L^2}{64|c|^2} + O\left(|c|^{-3}\right)$. This result and our numerical results both agree on a missing term of $-\frac{40L^2}{64|c|^2}$; thus we have concluded that this term is correct to add to our $s = 0$ solution. The agreement between our numerical solutions and Eq. (3.9) is shown in Fig. 3.2. This correction helps to verify the accuracy of our numerical results and corrects the $s = 0$ solution so that we may expand upon it for the $s \neq 0$ case.

Chapter 4: Fits for Non-Anomalous Sequences of $s \neq 0$

Following the confirmation of the numerical accuracy of our generated data and correcting the $s = 0$ solution, we began fitting our data for an accurate numerical fit of the prolate separation constants, ${}_sA_{\ell m}$. To get a fit in the asymptotic limit, we used the last 100 points of each sequence, which cover the values of $10^{4.5} < ic \leq 10^5$. The numeric fit for each sequence was separately determined by a least-square fitting method. For reasons stated in our qualitative analysis, we will restrict the fitting in this chapter to eigenvalues which exhibit linear leading-order behavior in the asymptotic limit. Since the asymptotic prolate eigenvalues were generally complex, we fit the real and imaginary components of each eigenvalue separately. We will be fitting all of our eigenvalue sequences with respect to the index $L' = L - {}_sN_{\ell m}$ for ${}_sN_{\ell m}$ being the number of anomalous eigenvalues present for m and s and smaller ℓ.

For the real components of ${}_sA_{\ell m}$, we assigned coefficients for each power of $|c|$ we would be fitting so that

$$\mathrm{Re}({}_sA_{\ell m}) = {}_0A_{\ell m} + B_1|c| + B_2 + B_3|c|^{-1} + B_4|c|^{-2} + B_5|c|^{-3}. \qquad (4.1)$$

Notice the inclusion of the corrected Flammer solution of ${}_0A_{\ell m}$ shown in Eq. (3.9). This inclusion serves as a base for the fit so that all of the terms we determine in this chapter will be corrections for general s. We made the substitution of $L \to L'$ in the analytic $s = 0$ solution to account for the presence of anomalous lines in the $s \neq 0$ cases. The accuracy of our numerical results typically became insufficient to determine numerical fits on the order of $|c|^{-3}$. As a result, we were unable to find the value of B_5, but B_5 was left in the model while fitting to improve the accuracy of the fits of the coefficients B_i for $i = 1, 2, 3, 4$.

As shown previously, the leading order behavior of the imaginary component is of order $|c|^{-1}$. Using C_i as coefficients, we used the following model to fit the imaginary components,

$$\mathrm{Im}({}_sA_{\ell m}) = C_1|c|^{-1} + C_2|c|^{-2} + C_3|c|^{-3}. \tag{4.2}$$

As before, the accuracy of the data only allows fits of order $|c|^{-2}$, but C_3 was included to allow for more accurate fitting of the other two coefficients.

We numerically determined the fits for each coefficient, B_i and C_i, one at a time. For each term we were fitting, we would determine the numeric fit for all values of m,

s, and L' that we generated. After fitting, we determined the value of the coefficients in terms of m, s, and L'. After determining an accurate value for the leading order coefficient being fit, this term would be added to our model and we would begin fitting the new leading order coefficient.

First, we found the coefficients of the real component of ${}_sA_{\ell m}$ starting with B_1. We found $B_1 = 0$ for all combinations of m, s, and L'. For example, the values fitted for the case of $m = 1$ can be seen in Table 4.1. This table is highly representative of all values of m we tested.

s	L'	B_1	Error
0	0	$1.61144973618034 \times 10^{-12}$	$2.92530698651516 \times 10^{-15}$
0	1	$3.60737656050638 \times 10^{-12}$	$9.58807336966575 \times 10^{-15}$
0	2	$8.00656830519925 \times 10^{-12}$	$1.84483293736652 \times 10^{-14}$
0	3	$1.44243599714087 \times 10^{-11}$	$2.35690235165235 \times 10^{-14}$
0	4	$2.21805586021287 \times 10^{-11}$	$3.35655417731396 \times 10^{-14}$
0	5	$2.44720102502109 \times 10^{-11}$	$4.36925436258825 \times 10^{-14}$
1	0	$1.00816101728544 \times 10^{-12}$	$3.03919295276373 \times 10^{-15}$
1	1	$9.59592542174497 \times 10^{-14}$	$9.64172462636152 \times 10^{-15}$
1	2	$2.02908639943997 \times 10^{-14}$	$1.42341613016550 \times 10^{-14}$
1	3	$4.49428126424873 \times 10^{-12}$	$2.09426353824868 \times 10^{-14}$
1	4	$8.82156959253786 \times 10^{-12}$	$2.13930661687694 \times 10^{-14}$
1	5	$8.22492976834100 \times 10^{-12}$	$3.41061212041317 \times 10^{-14}$
2	0	$1.10701134214716 \times 10^{-12}$	$2.85600726964254 \times 10^{-15}$
2	1	$3.68277288802595 \times 10^{-12}$	$1.01646043687812 \times 10^{-14}$
2	2	$2.03559255747130 \times 10^{-12}$	$1.28196708994457 \times 10^{-14}$
2	3	$6.24156971832138 \times 10^{-12}$	$2.30586437899687 \times 10^{-14}$
2	4	$1.08160722883971 \times 10^{-11}$	$2.26355134616265 \times 10^{-14}$
2	5	$1.07017234787836 \times 10^{-11}$	$4.27448027885524 \times 10^{-14}$

Table 4.1: Table of numerical fits of B_1 for select cases of $m = 1$.

After setting $B_1 = 0$ in Eq. (4.1), we began solving for B_2. Again using the values of $m = 1$, a sample set of numerical fits can be seen in Table 4.2. This additional behavior was found to be $B_2 = s^2 - s$. Notice that our fit for B_2 agrees with the symmetry shown in Eq. (1.2).

s	L'	B_2	Error
0	0	$1.390187268773607 \times 10^{-9}$	$1.372703725434353 \times 10^{-10}$
0	1	$9.006146865036666 \times 10^{-9}$	$5.170681626176239 \times 10^{-10}$
0	2	$3.057150124313022 \times 10^{-8}$	$9.329203880801399 \times 10^{-10}$
0	3	$1.109878074414446 \times 10^{-8}$	$1.178131538094029 \times 10^{-9}$
0	4	$2.290671890380051 \times 10^{-8}$	$1.631630426467578 \times 10^{-9}$
0	5	$4.788131999771475 \times 10^{-8}$	$2.001175597546363 \times 10^{-9}$
1	0	$5.620912397341866 \times 10^{-10}$	$2.905833165258755 \times 10^{-11}$
1	1	$1.376203432488877 \times 10^{-9}$	$1.240029237553002 \times 10^{-10}$
1	2	$4.643852170585592 \times 10^{-9}$	$1.707441352635793 \times 10^{-10}$
1	3	$1.242568793520602 \times 10^{-9}$	$2.293874887497271 \times 10^{-10}$
1	4	$1.064720064534127 \times 10^{-8}$	$2.745407398375354 \times 10^{-10}$
1	5	$4.724719959048166 \times 10^{-9}$	$4.430047757444075 \times 10^{-10}$
2	0	2.	$2.905833164444078 \times 10^{-11}$
2	1	2.	$1.158503491722719 \times 10^{-10}$
2	2	2.	$1.577567276497937 \times 10^{-10}$
2	3	2.	$2.443956715759321 \times 10^{-10}$
2	4	2.	$2.822038135462875 \times 10^{-10}$
2	5	2.	$3.990964604705679 \times 10^{-10}$

Table 4.2: Table of numerical fits of B_2 for select cases of $m = 1$.

Having determined a fit for B_2, this term was substituted into Eq. (4.1), and we began to fit B_3. Just as before, we were able to fit this behavior and found that $B_3 = (2L' + 1)\, s^2$. The fit of B_3 is demonstrated in Table 4.3 for the case of $m = 1$ and is representative of the broader data set.

s	L'	B_3	Error
0	0	-0.0000218456	$7.120289076355811 \times 10^{-6}$
0	1	-0.0000577089	0.0000260526
0	2	-0.000159854	0.0000504917
0	3	-0.000177989	0.0000625051
0	4	-0.000172193	0.0000793143
0	5	-0.000145381	0.000110382
1	0	1.	$3.989883484130801 \times 10^{-7}$
1	1	3.	$1.362804654126789 \times 10^{-6}$
1	2	5.	$2.123777662907833 \times 10^{-6}$
1	3	6.99999	$2.725609308253578 \times 10^{-6}$
1	4	9.	$3.771090743246509 \times 10^{-6}$
1	5	11.	$5.585836877783122 \times 10^{-6}$
2	0	4.	$3.836594072209420 \times 10^{-7}$
2	1	12.	$1.530368809407815 \times 10^{-6}$
2	2	20.	$1.830162164807040 \times 10^{-6}$
2	3	28.	$2.745243247210560 \times 10^{-6}$
2	4	36.	$3.602677824102283 \times 10^{-6}$
2	5	44.	$4.292110730421753 \times 10^{-6}$

Table 4.3: Table of numerical fits of B_3 for select cases of $m = 1$.

As before, the fit for B_3 was substituted into Eq. (4.1) and we began a fit for B_4. We determined that $B_4 = \left(3L'^2 + 3L' - 2m^2 - s^2 + \frac{3}{2}\right) s^2$. This fit is partially represented with the data from Table 4.4.

s	L'	B_4	Error
0	0	-0.000399697	0.00304732
0	1	-0.0000489715	0.010169
0	2	-0.00370892	0.0176161
0	3	0.0184527	0.0253875
0	4	-0.0110799	0.0307539
0	5	0.0053206	0.0373198
1	0	-1.50002	0.000038718
1	1	4.49998	0.000115671
1	2	16.4998	0.000191763
1	3	34.4998	0.000268246
1	4	58.4998	0.000348398
1	5	88.5	0.000426144
2	0	$-18.$	0.0000340286
2	1	5.99993	0.000116085
2	2	53.9997	0.000189132
2	3	126.	0.000273375
2	4	222.	0.000333509
2	5	342.	0.000429283

Table 4.4: Table of numerical fits of B_4 for select cases of $m = 1$.

Having fit the real component of ${}_sA_{\ell m}$ as accurately as our data would allow, we then moved on to fitting Eq. (4.2) for C_1 and C_2. Beginning with the fit for C_1, the first term in the expansion was determined to be $C_1 = 2ms^2$. This agrees with the fit shown in Table 4.5 for the case of $m = 1$.

s	L'	C_1	Error
0	0	0.	0.
0	1	0.	0.
0	2	0.	0.
0	3	0.	0.
0	4	0.	0.
0	5	0.	0.
1	0	2.	$3.392651077945907 \times 10^{-14}$
1	1	2.	$3.698566830855681 \times 10^{-13}$
1	2	2.	$2.165816635160056 \times 10^{-12}$
1	3	2.	$6.290143330802905 \times 10^{-12}$
1	4	2.	$1.367737860213665 \times 10^{-11}$
1	5	2.	$2.526912676799165 \times 10^{-11}$
2	0	8.	$1.096540873219888 \times 10^{-12}$
2	1	8.	$1.402410181696953 \times 10^{-12}$
2	2	8.	$3.987145757394644 \times 10^{-12}$
2	3	8.	$1.887313510420857 \times 10^{-11}$
2	4	8.	$4.707493655418772 \times 10^{-11}$
2	5	8.	$9.244112014192825 \times 10^{-11}$

Table 4.5: Table of numerical fits of C_1 for select cases of $m = 1$.

After substituting the value of C_1 into Eq. (4.2), we began fitting for C_2. This final iteration on fitting the non-anomalous data, shown representatively in Table 4.6, revealed that $C_2 = 4(2L' + 1)ms^2$.

s	L'	C_2	Error
0	0	0.	0.
0	1	0.	0.
0	2	0.	0.
0	3	0.	0.
0	4	0.	0.
0	5	0.	0.
1	0	4.	$3.92070910272162 \times 10^{-10}$
1	1	12.	$4.63473482038753 \times 10^{-9}$
1	2	20.	$2.71090099003680 \times 10^{-8}$
1	3	28.	$7.86958589314894 \times 10^{-8}$
1	4	36.	$1.71080372114226 \times 10^{-7}$
1	5	43.9999	$3.15978068495579 \times 10^{-7}$
2	0	16.	$1.36228373821577 \times 10^{-8}$
2	1	48.	$1.73600405585129 \times 10^{-8}$
2	2	80.	$4.96015363826839 \times 10^{-8}$
2	3	112.	$2.34559945831725 \times 10^{-7}$
2	4	144.	$5.84921927272765 \times 10^{-7}$
2	5	176.	$1.14819089667721 \times 10^{-6}$

Table 4.6: Table of numerical fits of C_2 for select cases of $m = 1$.

With these numeric solutions for the values of B_i and C_i, an accurate fit for the asymptotic series solution of ${}_sA_{\ell m}$ was determined. Keeping in mind symmetry from Eq. (1.1), even though we fit all variables as $|c|$, the odd powers of the imaginary component must actually depend upon the sign of c, and we represented this in the final equation. For non-anomalous eigenvalues, the power series solution was determined to be

$$
\begin{aligned}
{}_sA_{\ell m} =& |c|\left(2L'+1\right) - \left(2L'^2+2L'+3-4m^2+4s-4s^2\right)2^{-2} \\
& - \frac{1}{|c|}\left[2L'^3+3L'^2+\left(7-16m^2-32s^2\right)L'+3+8m^2-16s^2\right]2^{-4} - \frac{2ms^2}{c} \\
& - \frac{1}{|c|^2}\Big[5\left(L'^4+2L'^3+8L'^2+7L'+3\right)-48m^2\left(2L'^2+2L'+1\right) \\
& + 32\left(2s^4+4m^2s^2-6L's^2-6L'^2s^2-3s^2\right)+256\left(2L'+1\right)ms^2i\Big]2^{-6}+O\left(|c|^{-3}\right).
\end{aligned}
\tag{4.3}
$$

Equation (4.3) was found to agree with numerical fits found for $s = 2$ and $m = 0$ in Ref. [10], which fit only non-anomalous eigenvalues.

Chapter 5: Fits for Anomalous Sequences

In this chapter, we will work to include the behavior of the anomalous line sequences in our numeric fits for the prolate asymptotic eigenvalues. In order to do this, we first set out to understand which combinations of m, s, and L lead to anomalous eigenvalue sequences. Then, we wanted to fit these anomalous lines. From Ch. 4, we already know that for a sequence to be anomalous, the real component of ${}_sA_{\ell m}$ will exhibit quadratic leading order behavior in agreement with Eq. (2.1). We also know that the imaginary component of an anomalous line will have linear leading-order behavior.

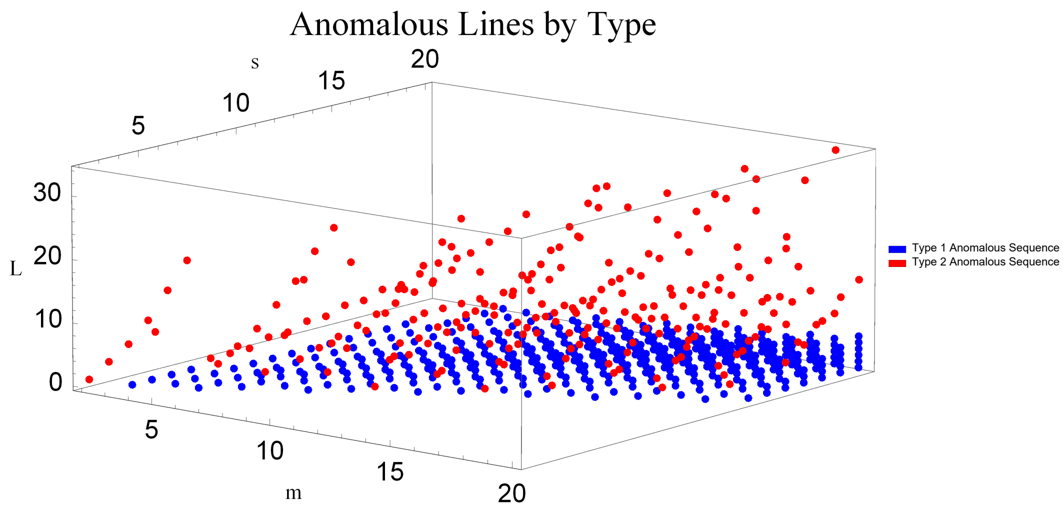

Figure 5.1: Combinations of m, s, and ℓ which yield anomalous lines. Note the difference in the distribution of the type 1 sequences vs. the type 2 sequences. The type 1 anomalous eigenvalue sequences are clustered near low values of L while the type 2 anomalous sequences are more evenly distributed.

We did not find any rule that precisely predicted which combinations of m, s, and L were anomalous, but we found some general trends. For the combinations of m, s, and L checked in this study, it was always true that any sequence with $|m| < 2$ or $|s| < \frac{2|m|}{3} + 1$ was not anomalous. It was also always true that eigenvalues which obeyed the constraints of $L \leq \frac{5|s|}{6} - \frac{|m|}{2} - 1$ and $L \leq \frac{|m|}{3} - \frac{|s|}{30} - \frac{10}{13}$ were found to be anomalous. We decided to label the anomalous lines which adhered to these constraints as type 1 anomalous lines. For all other combinations of m, s, and L, we were unable to find a method for determining which lines would be anomalous. We labeled the rest of these anomalous lines as type 2. Figure 5.1 shows the anomalous line combinations separated by type in the space of combinations of m, s, and L checked in this study.

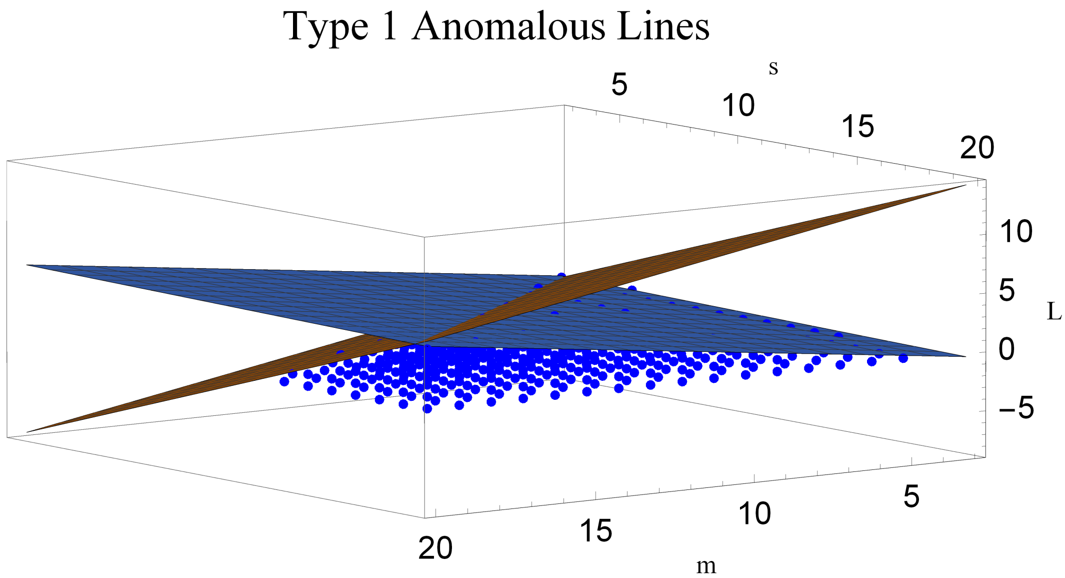

Figure 5.2: The two planes illustrate the constraints on type 1 anomalous sequences. All points in this figure are the type 1 anomalous lines, and all of these points fall on or under the two planes which represent $L \leq \frac{5|s|}{6} - \frac{|m|}{2} - 1$ and $L \leq \frac{|m|}{3} - \frac{|s|}{30} - \frac{10}{13}$.

One can visualize the constraints that leads to type 1 anomalous lines in Fig. 5.2. Of the 670 anomalous lines that we found, 441 of them were type 1. A full list of combinations of m, s, and L which lead to anomalous lines separated by type can be found in Appendices A and B. Since type 1 anomalous lines appear for low values of L and we primarily checked low values of L, we cannot draw a conclusion with regards to if type 1 anomalous lines are generally more common than type 2 anomalous lines.

Next, we moved on to determining an asymptotic prolate fit for the anomalous eigenvalue sequences. When looking at the linear and constant order behavior of the anomalous sequences, it became evident that the type 1 anomalous lines agreed with the first three terms of the analytic power-series expansion for the asymptotic oblate eigenvalue solutions given in Eq. (1.4). The even and odd parity in $|c|$ for the real and imaginary components respectively is conveniently explained by the dependence upon the phase of c of Eq. (1.4). Starting with the order c^{-1} term, there is distinct disagreement between the numeric type 1 anomalous solutions and Eq. (1.4), which we will fit later in this chapter.

It turns out that the type 2 anomalous lines also fit Eq. (1.4) out to constant order with a noticeable difference in the fit behavior. Similarly to how we had to adjust the label of L to L' for the non-anomalous eigenvalues, we must shift the label of L for the type 2 anomalous eigenvalue sequences. We chose the new label of L^* and this shift goes as $L \to L^* = {}_sN_{\ell m}$. This relabeling means that for a given combination of m and s, the anomalous eigenvalue sequence with the lowest value of L will be $L^* = 0$—the next lowest value of L shall be $L^* = 1$ and so on. Due to the constraints on type 1 anomalous lines, it turns out that for type 1 anomalous eigenvalue sequences $L = L^*$, and thus this label can also be used for the type 1 sequences.

This shift to L^* means that all anomalous sequences, regardless of type, obey

$$ {}_sA_{\ell m,anomalous} = -c^2 + 2{}_sq^*_{\ell m}c - \frac{1}{2}\left({}_sq^{*2}_{\ell m} - m^2 + 2s + 1\right) + O\left(c^{-1}\right) \tag{5.1} $$

for

$$ {}_sq^*_{\ell m} = 2L^* + |m-s| - s + 1. \tag{5.2} $$

Notice the condition on Eq. (1.8) means that all combinations of m, s, and L generated in this study would use ${}_sq_{\ell m}$ for the condition from Eq. (1.8) rather than Eq. (1.7). Thus, we are unable to determine if we need two different definitions of ${}_sq^*_{\ell m}$ for anomalous lines outside our domain of solutions.

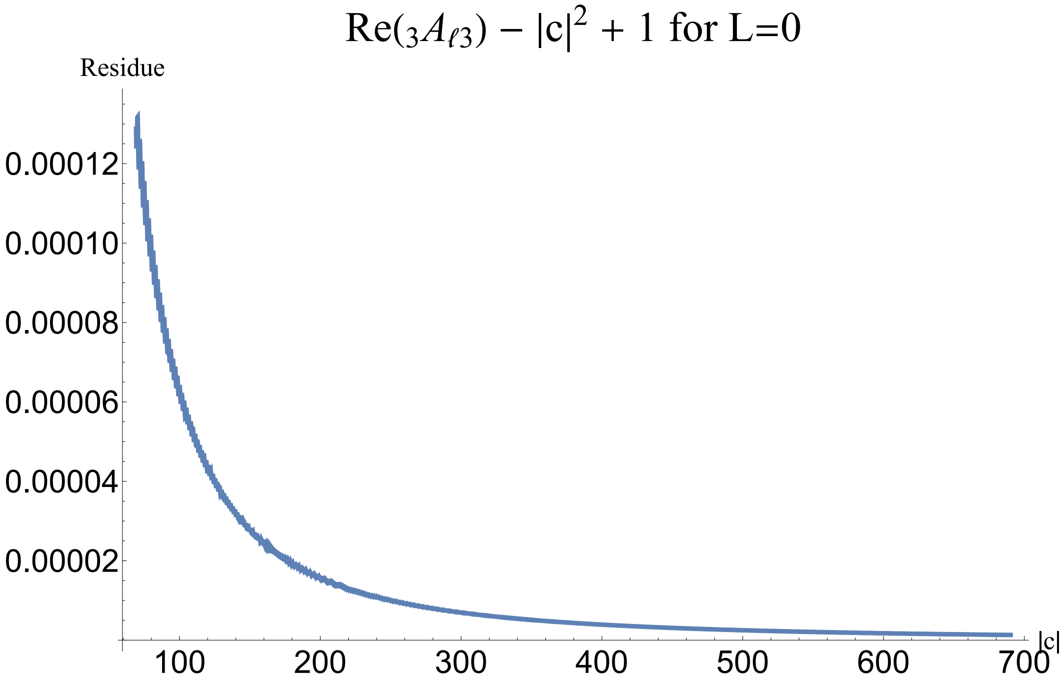

Figure 5.3: Residue of the real component of the type 1 anomalous sequence ${}_3A_{\ell 3}$ for $L = 0$ subtracting the quadratic and constant order behavior.

Starting at order c^{-1}, the type 1 and type 2 anomalous lines appear to follow two different polynomial fits. Figure 5.3 shows the real component of the type 1 anomalous sequence of ${}_3A_{\ell 3}$ for $L = 0$ after removing the quadratic and constant order real behavior. After the constant order term, the next term in the solution for $L = 0$ fits as order c^{-2} with no behavior of order c^{-1}. This behavior is shared by all type 1 anomalous eigenvalue sequences.

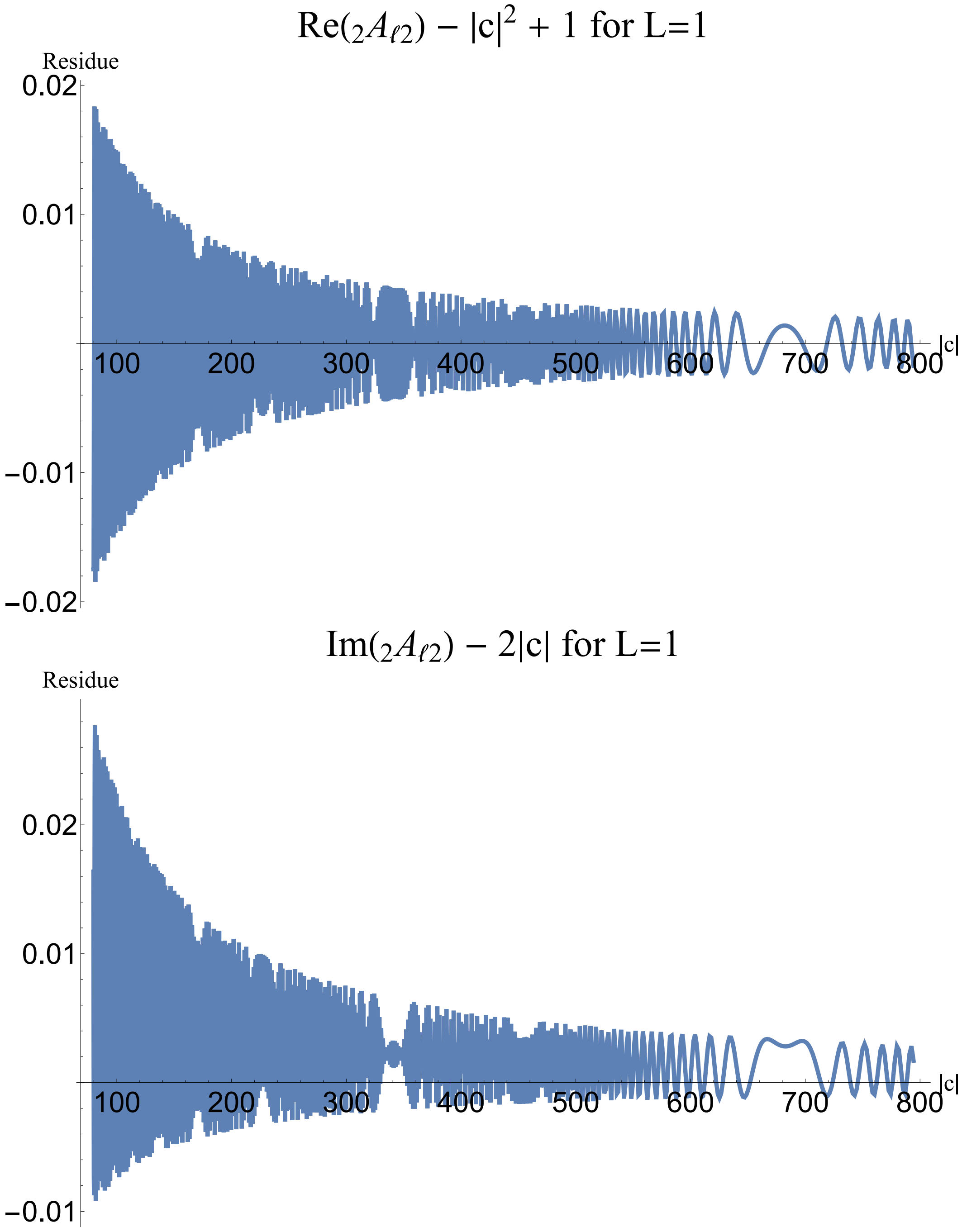

Figure 5.4: Residue of the real and imaginary components of the type 2 anomalous sequence $_2A_{\ell 2}$ for $L = 1$ subtracting the behavior at constant order and above in $|c|$. Note the oscillatory behavior which differs from the behavior shown in Fig. 5.3.

Figure 5.4 shows the real and imaginary residues of the type 2 anomalous line

${}_2A_{\ell 2}$ for $L = 1$ after subtracting off the behavior of constant order and higher. This behavior greatly contrasts with the type 1 anomalous sequence behavior shown in Fig. 5.3. A log-log plot shows that the oscillatory behavior is of order $|c|^{-1}$ in both real and imaginary components of the residue. This oscillatory behavior is shared by all type 2 sequences.

It is noteworthy that the type 1 anomalous eigenvalue sequences, which did not exhibit the oscillatory behavior of order $|c|^{-1}$, also did not exhibit the wobbling behavior we mentioned for some anomalous lines shown in Figs. 2.8 and 2.10. All type 2 anomalous eigenvalues surveyed showed some form of oscillatory behavior of order $|c|^{-1}$ akin to that shown in Fig. 5.4 and also exhibited the wobbling behavior described before. This may indicate that there is some link between the two.

For type 2 anomalous sequences the oscillatory behavior prevents us from extending Eq. (5.1) to order c^{-1} due to an inability to arrive at reliable numerical fits. Thus, we proceeded to attempt fitting the type 1 anomalous sequences. Just as for the non-anomalous lines, we used the final 100 points in each type 1 anomalous sequence to ensure that points used for fitting were sufficiently far in the asymptotic regime.

We then used a model of

$$ {}_sA_{\ell m} = -c^2 + 2{}_sq^*_{\ell m}c - \frac{1}{2}\left({}_sq^{*2}_{\ell m} - m^2 + 2s + 1\right) + D_1c^{-1} + D_2c^{-2} + D_3c^{-3} + D_4c^{-4}. \quad (5.3) $$

We started with the highest order term, D_1. A small sample of numeric fits for D_1 of the type 1 anomalous sequences can be seen in Table 5.1.

m	s	L^*	${}_sq^*_{\ell m}$	D_1	Error
3	3	0	-2	1.24999396	$2.7886449143 \times 10^{-6}$
3	4	0	-2	3.00003810	0.0000168474
3	5	0	-2	5.24990466	0.0000604800
3	6	0	-2	8.00028868	0.0001628709
4	4	0	-3	1.74999999	$1.6804714167 \times 10^{-10}$
4	5	0	-3	3.99999999	$2.2306479145 \times 10^{-10}$
4	6	0	-3	6.75000000	$8.4059148595 \times 10^{-10}$
4	7	0	-3	9.99999996	$9.9274253335 \times 10^{-8}$
4	8	0	-3	13.7499998	$2.7294211243 \times 10^{-7}$
4	9	0	-3	17.9999998	$6.3754859270 \times 10^{-7}$
4	10	0	-3	22.7499993	$1.3758337084 \times 10^{-6}$
4	11	0	-3	27.9999997	$9.0687773061 \times 10^{-6}$
4	12	0	-3	33.7499915	0.0000163378
4	13	0	-3	39.9999982	0.0000251166
4	14	0	-3	46.7499818	0.0000426685
4	15	0	-3	53.9999673	0.0000712527
4	16	0	-3	61.7499924	0.0001086124
5	4	0	-2	6.99975657	0.0001170334

Table 5.1: Table of fits of D_1 for select type 1 anomalous eigenvalue sequences.

If we find the difference between our polynomial fit of the data in Table 5.1 and the term for the analytic oblate solutions, A_1, which is shown in Eq. (1.5), we find that

$D_1 - A_1 = \frac{1}{8}s^2({}_sq^*_{\ell m} + m)$. This demonstrates that our numerical type 1 anomalous eigenvalue solutions do not exactly fit the analytic oblate power-series solution derived in Ref. [7] once we fit past constant order in c.

As with the non-anomalous numerical fits, we added our newly fit term of D_1 to Eq. (5.3) and began to fit for the next term, D_2. The term from the analytic power-series expression for the asymptotic oblate case of order $|c|^{-2}$ is A_2, which is shown in Eq. (1.6). We determined that $D_2 - A_2 = \frac{1}{8}s^2\left(({}_sq^*_{\ell m} + 1)^2 + 1\right)$, which again shows only a slight but distinguishable difference in our numerical fit of the type 1 anomalous sequences and Eq. (1.4). A sample list of numeric fits for D_2 can be found in Table 5.2.

m	s	L^*	${}_sq^*_{\ell m}$	D_2	Error
3	3	0	-2	0.623898302078	0.0017244867790978
3	4	0	-2	1.500231687006	0.0104484835898758
3	5	0	-2	2.618153321697	0.0368447543296024
3	6	0	-2	3.995300986577	0.0978273216685553
4	4	0	-3	1.749988815883	0.0000209290823329
4	5	0	-3	3.999977407912	0.0000201373121023
4	6	0	-3	6.749985083639	0.0000207370894613
4	7	0	-3	9.999992873453	0.0000244567737245
4	8	0	-3	13.750019105424	0.0000672839104980
4	9	0	-3	17.999966332517	0.0001580777026734
4	10	0	-3	22.749950144191	0.0003494496999696
4	11	0	-3	27.999554149173	0.0016683488235863
4	12	0	-3	33.749348080236	0.0031025676111110
4	13	0	-3	40.001256822186	0.0049285181927592
4	14	0	-3	46.747928952831	0.0083848487908798
4	15	0	-3	54.002992070813	0.0136677482926649
4	16	0	-3	61.754577780630	0.0214581995690651
5	4	0	-2	3.470201796616	0.0719008117082672

Table 5.2: Table of fits of D_2 for select type 1 anomalous eigenvalue sequences.

D_2 is the final coefficient which we had sufficient numerical accuracy to reliably determine. Thus, we concluded that the fit for the type 1 anomalous eigenvalue sequences is

$$\begin{aligned}
{}_sA_{\ell m,type1} =& - c^2 + 2{}_sq^*_{\ell m}c - \frac{1}{2}\left[{}_sq^{*2}_{\ell m} - m^2 + 2s + 1\right] \\
& - \frac{1}{8c}\left[{}_sq^{*3}_{\ell m} - m^2\,{}_sq^*_{\ell m} + {}_sq^*_{\ell m} - 2s^2({}_sq^*_{\ell m} + m)\right] \\
& - \frac{1}{64c^2}\Big[5\,{}_sq^{*4}_{\ell m} - \left(6m^2 - 10\right)\,{}_sq^{*2}_{\ell m} + m^4 - 2m^2 \\
& - 4s^2\left({}_sq^{*2}_{\ell m} - m^2 - 1\right) + 1 - 8s^2\left(({}_sq^*_{\ell m} + 1)^2 + 1\right)\Big] + O\left(c^{-3}\right).
\end{aligned} \tag{5.4}$$

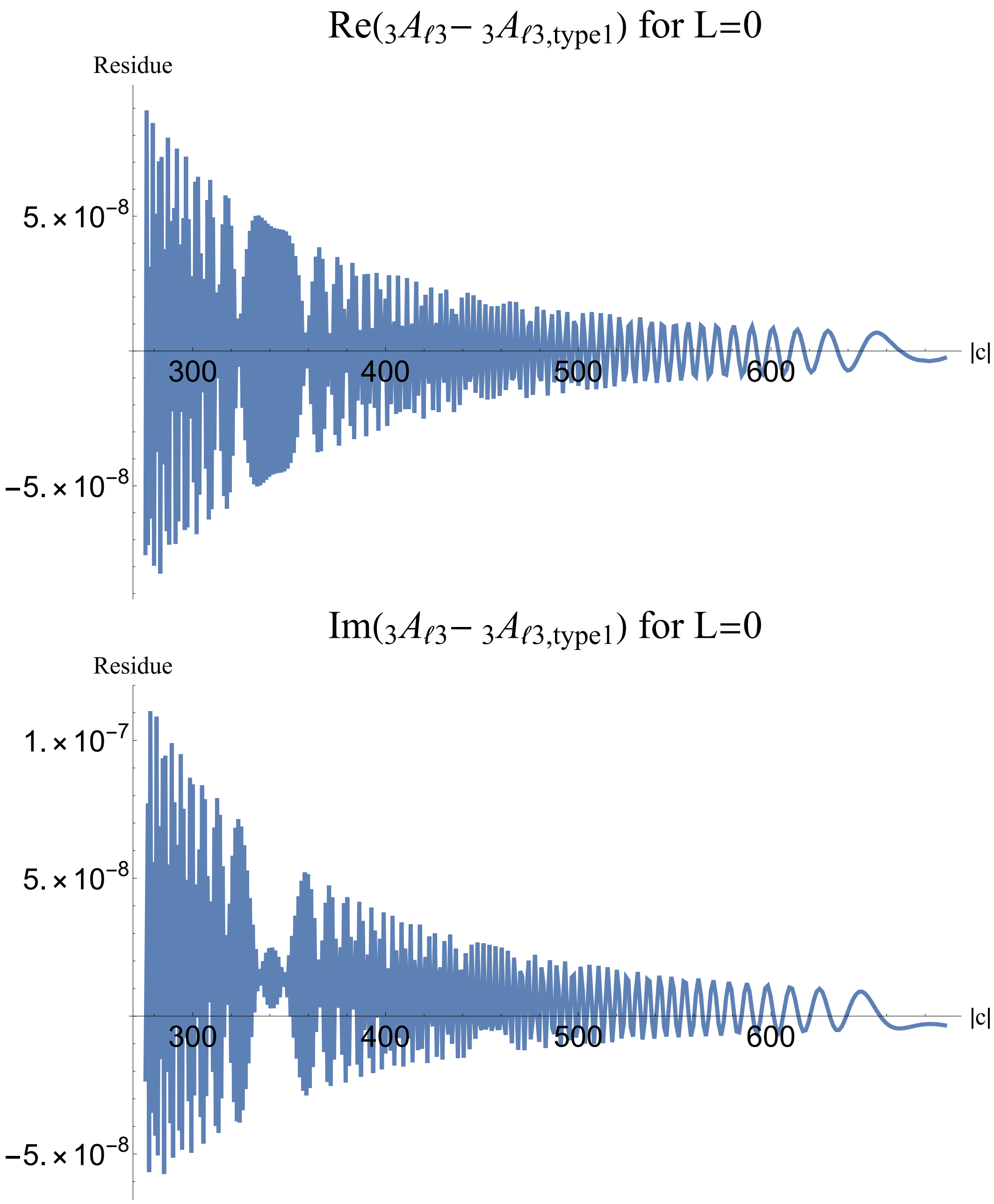

Figure 5.5: Residue of the real and imaginary components of the type 1 anomalous sequence ${}_3A_{\ell 3}$ for $L = 0$ after subtracting Eq. (5.4). Note that there is new oscillatory behavior of order $|c|^{-3}$ present, similar to the behavior seen in type 2 anomalous sequences at order $|c|^{-1}$ shown in Fig. 5.4.

Figure 5.5 shows a sample residue of the type 1 anomalous line of ${}_3A_{\ell 3}$ for $L = 0$

after removing the behavior from Eq. (5.4). Note that this is the same sequence as shown in Fig. 5.3 after removing some leading order terms. Both the real and imaginary component of this eigenvalue sequence has oscillatory behavior of order $|c|^{-3}$, and this general behavior is consistent with all type 1 anomalous sequences. This behavior is of a very similar form to the oscillatory behavior of type 2 anomalous sequences at order c^{-1} shown in Fig. 5.4. This oscillatory behavior prevents us from determining reliable numerical fits for D_3 and D_4. It is evident that the key to extending the fits for the type 1 and type 2 anomalous sequences lies in determining the nature of the oscillatory behavior present in each or analytically deriving corrections for anomalous prolate eigenvalues.

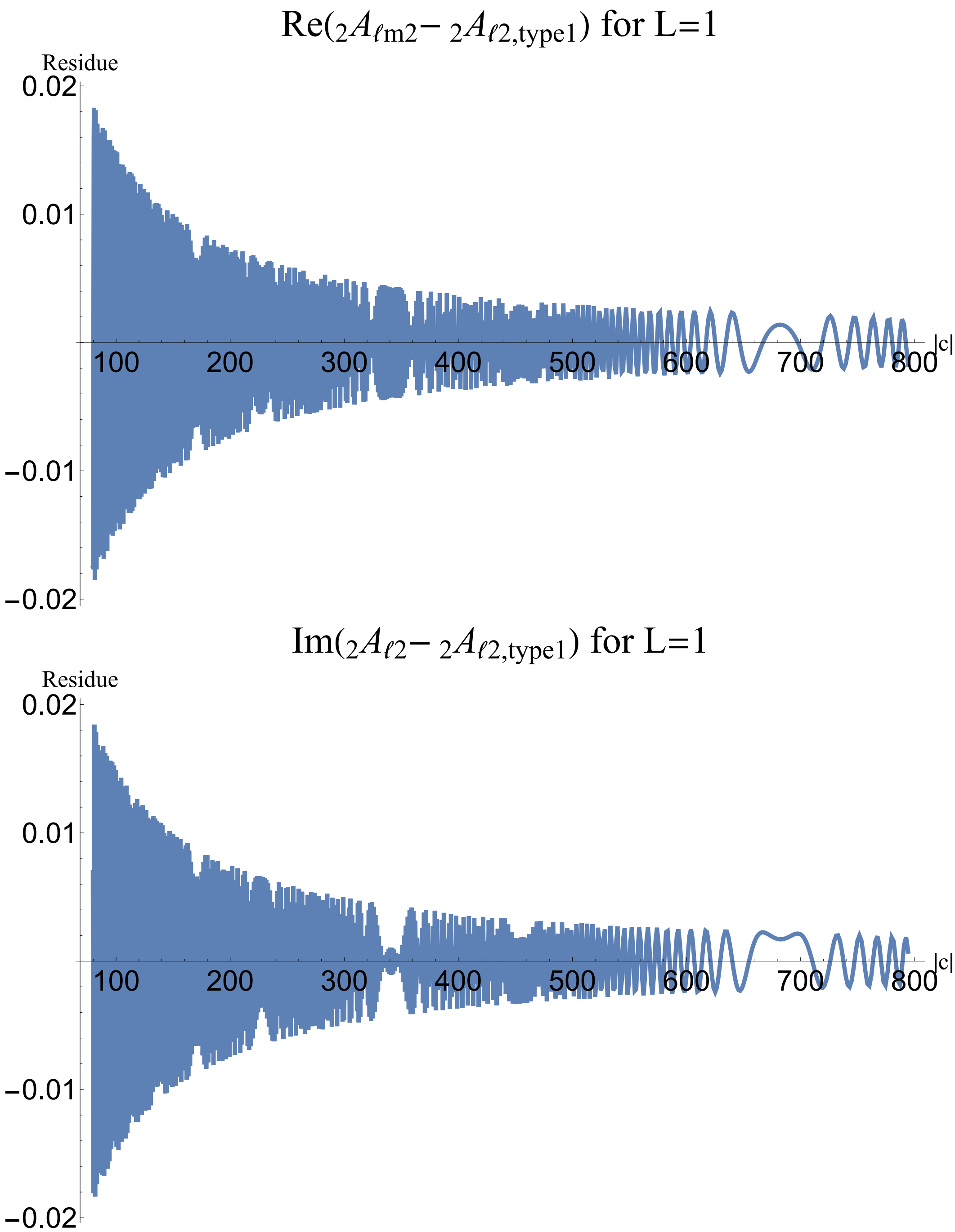

Figure 5.6: Residue of the real and imaginary components of the type 2 anomalous line ${}_2A_{\ell 2}$ after subtracting out the the type 1 anomalous behavior given in Eq. (5.4).

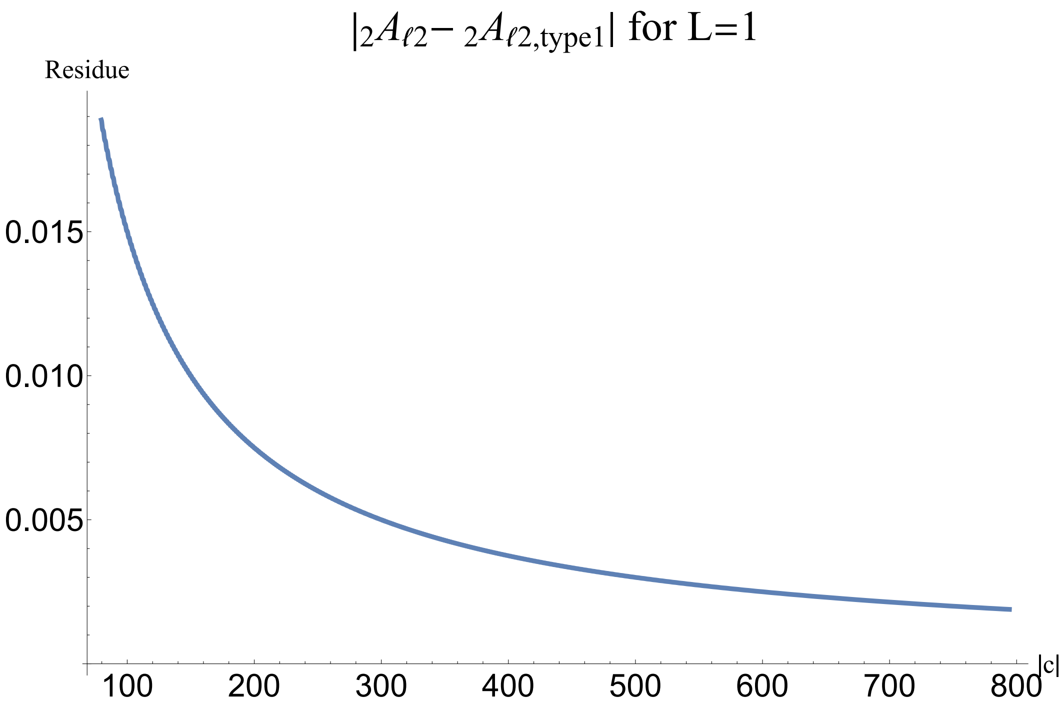

Figure 5.7: Magnitude of the residue of the type 2 anomalous line ${}_2A_{\ell 2}$ after subtracting out the the type 1 anomalous behavior given in Eq. (5.4). Once removing all non-oscillatory behavior, the magnitude of the residue is of order $|c|^{-1}$ and the shape of the magnitude of the residue indicates that the oscillatory behavior in Fig. 5.6 seems to be due to a complex exponential term.

It appears that the type 2 anomalous eigenvalue sequences also partially follow the numerical fit of the type 1 solutions given in Eq. (5.4). The only notable exception would be the oscillatory behavior shown to be present for the type 2 anomalous sequences. Figure 5.6 shows the real and imaginary components of the residue of the same type 2 anomalous eigenvalue sequence shown in Fig. 5.4 after removing the behavior from Eq. (5.4). Notice that the two components appear to oscillate more closely around zero than in Fig. 5.4. Figure 5.7 shows the magnitude of the residue. These additional terms seem to have removed the dominant non-oscillatory behavior, which allows us to more cleanly take the magnitude of the residue. This plot of the magnitude of the residue is of order $|c|^{-1}$ and demonstrates how this oscillatory behavior appears to be due to a complex exponential term which we were unable to determine. It seems reasonable to assume that the oscillatory behavior of the type 1 sequences shown in Fig. 5.5 is also due to a complex exponential term of order $|c|^{-3}$, but we cannot be sure with our current polynomial fit of type 1 sequences.

Chapter 6: Conclusions

This study was a high-accuracy numerical analysis of solutions to the angular Teukolsky equation in the asymptotic prolate limit for all integer combinations of $-10 \leq s \leq 20$, $-10 \leq m \leq 20$, and $L \leq 15$. As shown in Fig. 2.11, we noted the presence of lines with quadratic leading order behavior, which we refer to as anomalous eigensolutions of Eq. (0.3). The presence of the anomalous lines caused us to determine three different numeric fits for the power-series expansion in $|c|$ for eigenvalue solutions to Eq. (0.3)—one for the non-anomalous eigenvalue solutions and one for each of two types of anomalous eigenvalue solutions. The non-anomalous eigenvalue solutions agreed with previously explored analytic and numeric eigensolutions, with the exception of a correction we derived for $s = 0$ solutions shown in Eq. (3.9). Our numeric fit for general s is to higher-order in $|c|$ or is more general than previous numeric fits for prolate ${}_sA_{\ell m}$. Our non-anomalous numerical fit is displayed in Eq. (4.3).

With respect to the anomalous eigenvalue solutions, we determined a rule to partially determine which eigensolutions would be anomalous. We also found agreement between all numeric anomalous prolate solutions and the analytic oblate power-series expansion out to constant order, given in Eq. (5.1). In this categorization and fitting of the anomalous eigenvalue solutions, we were able to group the anomalous sequences into two categories based on combinations of m, s, and L, as well as behavior for the power-series expansion of the eigenvalue solutions at order c^{-1}. For the type 1 anomalous eigenvalue sequences, we were able to use Eq. (1.4) as a base to extend the anomalous power-series expansion to order c^{-2}. This power-series expansion is shown in Eq. (5.4). We were able to determine that the type 2 anomalous eigenvalue sequences also partially agreed with Eq. (5.4), with a correction needed for a complex exponential term of order c^{-1}. Our justification for the existence of such a term is best demonstrated by Fig. 5.6.

The primary results of interest from this work are the numeric fits of asymptotic prolate values of ${}_sA_{\ell m}$, particularly for non-anomalous solutions. Our fit for ${}_sA_{\ell m}$ can hopefully reduce the numerical load required for works which require solutions to Eq. (0.3) in the future. We also hope that our numeric fit may provide some direction for future attempts to analytically generalize solutions to Eq. (0.3).

The other interesting result from this work is the existence of the anomalous eigenvalue solutions to Eq. (0.3) in the asymptotic prolate case, which have not been previously predicted nor explored. We would be interested in better understanding the properties of the anomalous eigenvalue solutions. In particular, we would like to know a general rule for which eigenvalue lines will be anomalous and how many anomalous lines one should expect for a given combination of m and s. Based on how the anomalous eigenvalue sequences fit to Eq. (5.1), it is possible that there are a countably infinite number of anomalous lines and each anomalous eigensolution may correlate to an eigensolution of the analytic oblate case. If this is indeed true, we would be very interested in knowing if there are solutions in the case of complex c which also partially fit Eq. (1.4). Both of these questions provide useful information for the possibility of constructing corrections to Eq.(1.4), starting at order c^{-1}, that could generalize it for complex c.

Since we only found anomalous eigenvalue solutions for values of $|s| \geq 2$, and most applications of anomalous eigenvalue solutions to Eq. (0.3) are for values of $-2 \leq s \leq$

2, the $s = \pm 2$ anomalous eigenvalues will likely be most relevant. From a physical standpoint, the usefulness of anomalous lines is questionable and will likely depend upon the prevalence of wave equations which require asymptotic prolate solutions and if anomalous spin-weighted spheroidal functions will make significant contributions to these wave equations compared to the non-anomalous solutions of ${}_sS_{\ell m}$. The case of $s = \pm 2$ is simplified greatly with regards to anomalous eigensolutions since we found only four anomalous eigensolutions for this case: ${}_2A_{32}$, ${}_{-2}A_{32}$, ${}_2A_{3(-2)}$, and ${}_{-2}A_{3(-2)}$.

It is worth noting that the anomalous eigenvalue sequences required a significantly larger matrix size to compute for our error threshold than their non-anomalous counterparts. Including the anomalous eigensolutions in the data we collected greatly increased the computational work required to find solutions as well as decreased the efficiency in storing and handling our data. If one wished to extend our non-anomalous solutions given in Eq. (4.3), this could be done with greater efficiency by not tracking the anomalous eigenvalue solutions. Thus, our solutions could be extended with less computational work and smaller data. The presence of the anomalous solutions in the prolate asymptotic case leaves room to explore if there are eigenvalue solutions which partially agree with the analytic oblate solution given in Eq. (1.4) for general complex c.

Bibliography

[1] B. P. Abbott, et al. Observation of gravitational waves from a binary black hole merger. *Phys. Rev. Lett.*, 116:061102, Feb. 2016.

[2] James M. Bardeen and William H. Press. Radiation fields in the Schwarzschild background. *Journal of Mathematical Physics*, 14(1):7–19, 1973.

[3] James M. Bardeen, William H. Press, and Saul A. Teukolsky. Rotating Black Holes: Locally Nonrotating Frames, Energy Extraction, and Scalar Synchrotron Radiation. *Astrophys. J.*, 178:347–370, Dec. 1972.

[4] Emanuele Berti, Vitor Cardoso, and Marc Casals. Eigenvalues and eigenfunctions of spin-weighted spheroidal harmonics in four and higher dimensions. *Phys. Rev. D*, 73:024013, Jan. 2006.

[5] Emanuele Berti, Vitor Cardoso, and Shijun Yoshida. Highly damped quasinormal modes of Kerr black holes: A complete numerical investigation. *Phys. Rev. D*, 69:124018, Jun. 2004.

[6] Miguel A. Blanco, M. Flörez, and M. Bermejo. Evaluation of the rotation matrices in the basis of real spherical harmonics. *J. Mol. Struct. (Theochem)*, 419(1):19 – 27, 1997.

[7] R. A. Breuer, Jr. Ryan, M. P., and S. Waller. Some Properties of Spin-Weighted Spheroidal Harmonics. *Proc. R. Soc. Lond. A*, 358(1692):71–86, Dec. 1977.

[8] Marc Casals and Adrian C. Ottewill. High frequency asymptotics for the spin-weighted spheroidal equation. *Phys. Rev. D*, 71:064025, Mar. 2005.

[9] Subrahmanyan Chandrasekhar. On the equations governing the perturbations of the Schwarzschild black hole. *Proc. R. Soc. Lond. A*, 343(1634):289–298, 1975.

[10] Gregory B. Cook, Luke S. Annichiarico, and Daniel J. Vickers. Unknown branch of the total-transmission modes for the Kerr geometry. *Phys. Rev. D*, 99:024008, Jan. 2019.

[11] Gregory B. Cook and Maxim Zalutskiy. Modes of the Kerr geometry with purely imaginary frequencies. *Phys. Rev. D*, 94:104074, Nov. 2016.

[12] S. Detweiler and Subrahmanyan Chandrasekhar. On resonant oscillations of a

rapidly rotating black hole. *Proc. R. Soc. Lond. A*, 352(1670):381–395, 1977.

[13] Valeria Ferrari and Bahram Mashhoon. New approach to the quasinormal modes of a black hole. *Phys. Rev. D*, 30:295–304, Jul. 1984.

[14] Bartolomeu D B Figueiredo. On some solutions to generalized spheroidal wave equations and applications. *Journal of Physics A: Mathematical and General*, 35(12):2877–2906, Mar. 2002.

[15] Carson Flammmer. Spheroidal wave functions, 1957.

[16] Scott A. Hughes. Evolution of circular, nonequatorial orbits of Kerr black holes due to gravitational-wave emission. *Phys. Rev. D*, 61:084004, Mar. 2000.

[17] William Krivan, Pablo Laguna, Philippos Papadopoulos, and Nils Andersson. Dynamics of perturbations of rotating black holes. *Phys. Rev. D*, 56(6), Sep. 1997.

[18] B. Larsson, T. Levitina, and E. J. Brändas. On prolate spheroidal wave functions for signal processing. *Int. J. Quant. Chem.*, 85(4-5):392–397, 2001.

[19] E.W. Leaver. An Analytic representation for the quasi normal modes of Kerr

black holes. *Proc. Roy. Soc. Lond. A*, 402:285–298, 1985.

[20] Ramön Löpez-Alemän, Gaurav Khanna, and Jorge Pullin. Perturbative evolution of particle orbits around Kerr black holes: time-domain calculation. *Classical Quantum Gravity*, 20(14), Jul. 2003.

[21] Alec Maassen van den Brink. Analytic treatment of black-hole gravitational waves at the algebraically special frequency. *Phys. Rev. D*, 62:064009, Aug. 2000.

[22] Hiroyuki Nakano, Yosef Zlochower, Carlos O. Lousto, and Manuela Campanelli. Intermediate-mass-ratio black hole binaries. ii. modeling trajectories and gravitational waveforms. *Phys. Rev. D*, 84:124006, Dec. 2011.

[23] Hans-Peter Nollert and Bernd G. Schmidt. Quasinormal modes of Schwarzschild black holes: Defined and calculated via Laplace transformation. *Phys. Rev. D*, 45:2617–2627, Apr. 1992.

[24] Hisashi Onozawa. Detailed study of quasinormal frequencies of the Kerr black hole. *Phys. Rev. D*, 55(6):3593–3602, Mar. 1997.

[25] Tullio Regge and John A. Wheeler. Stability of a Schwarzschild singularity. *Phys. Rev.*, 108:1063–1069, Nov. 1957.

[26] Misao Sasaki and Takashi Nakamura. Gravitational Radiation from a Kerr Black Hole. I. Formulation and a Method for Numerical Analysis. *Prog. Theor. Phys.*, 67(6):1788–1809, 06 1982.

[27] Misao Sasaki and Hideyuki Tagoshi. Analytic black hole perturbation approach to gravitational radiation. *Phys. Rev. D*, Nov. 2003.

[28] Saul A. Teukolsky. Perturbations of a Rotating Black Hole. I. Fundamental Equations for Gravitational, Electromagnetic, and Neutrino-Field Perturbations. *Astrophys. J.*, 185:635–648, Oct. 1973.

[29] Daniel J. Vickers. Determining the asymptotic expansion of prolate spin-weighted spheroidal eigenvalues, May 2018. Honor's Thesis.

[30] Frank J. Zerilli. Effective potential for even-parity Regge-Wheeler gravitational perturbation equations. *Phys. Rev. Lett.*, 24:737–738, Mar. 1970.

Appendix A: List of Type 1 Anomalous Lines

The following table is a list of which combinations of m, s, and L lead to type 1 anomalous eigenvalue sequences. These sequences obey constraints given in Ch. 5, exhibit no deflection behavior similar to that seen in Fig. 2.8, obey the polynomial fit given in Eq. (5.4), and have oscillatory of order $|c|^{-3}$ as shown in Fig. 5.5.

m	s	L	m	s	L	m	s	L	m	s	L
3	3	0	3	4	0	3	5	0	3	6	0
4	4	0	4	5	0	4	6	0	4	7	0
4	8	0	4	9	0	4	10	0	4	11	0
4	12	0	4	13	0	4	14	0	4	15	0
4	16	0	5	4	0	5	5	0	5	6	0
5	7	0	5	8	0	5	9	0	5	10	0
5	11	0	5	12	0	5	13	0	5	14	0
5	15	0	5	16	0	5	17	0	5	18	0
5	19	0	5	20	0	6	5	0	6	6	1
6	6	0	6	7	1	6	7	0	6	8	0
6	9	0	6	10	0	6	11	0	6	12	0
6	13	0	6	14	0	6	15	0	6	16	0
6	17	0	6	18	0	6	19	0	6	20	0
7	6	0	7	7	1	7	7	0	7	8	1
7	8	0	7	9	1	7	9	0	7	10	1
7	10	0	7	11	1	7	11	0	7	12	0
7	13	0	7	14	0	7	15	0	7	16	0
7	17	0	7	18	0	7	19	0	7	20	0
8	6	0	8	7	0	8	8	1	8	8	0
8	9	1	8	9	0	8	10	1	8	10	0
8	11	1	8	11	0	8	12	1	8	12	0
8	13	1	8	13	0	8	14	1	8	14	0
8	15	1	8	15	0	8	16	1	8	16	0
8	17	0	8	18	0	8	19	0	8	20	0
9	7	0	9	8	1	9	8	0	9	9	1

9	9	0	9	10	1	9	10	0	9	11	1
9	11	0	9	12	1	9	12	0	9	13	1
9	13	0	9	14	1	9	14	0	9	15	1
9	15	0	9	16	1	9	16	0	9	17	1
9	17	0	9	18	1	9	18	0	9	19	1
9	19	0	9	20	1	9	20	0	10	8	0
10	9	1	10	9	0	10	10	2	10	10	1
10	10	0	10	11	2	10	11	1	10	11	0
10	12	2	10	12	1	10	12	0	10	13	1
10	13	0	10	14	1	10	14	0	10	15	1
10	15	0	10	16	1	10	16	0	10	17	1
10	17	0	10	18	1	10	18	0	10	19	1
10	19	0	10	20	1	10	20	0	11	8	0
11	9	0	11	10	1	11	10	0	11	11	2
11	11	1	11	11	0	11	12	2	11	12	1
11	12	0	11	13	2	11	13	1	11	13	0
11	14	2	11	14	1	11	14	0	11	15	2
11	15	1	11	15	0	11	16	1	11	16	0
11	17	1	11	17	0	11	18	1	11	18	0
11	19	1	11	19	0	11	20	1	11	20	0
12	9	0	12	10	1	12	10	0	12	11	1
12	11	0	12	12	2	12	12	1	12	12	0
12	13	2	12	13	1	12	13	0	12	14	2
12	14	1	12	14	0	12	15	2	12	15	1
12	15	0	12	16	2	12	16	1	12	16	0
12	17	2	12	17	1	12	17	0	12	18	2
12	18	1	12	18	0	12	19	2	12	19	1
12	19	0	12	20	2	12	20	1	12	20	0
13	10	0	13	11	1	13	11	0	13	12	2
13	12	1	13	12	0	13	13	3	13	13	2
13	13	1	13	13	0	13	14	2	13	14	1
13	14	0	13	15	2	13	15	1	13	15	0
13	16	2	13	16	1	13	16	0	13	17	2
13	17	1	13	17	0	13	18	2	13	18	1
13	18	0	13	19	2	13	19	1	13	19	0
13	20	2	13	20	1	13	20	0	14	10	0
14	11	0	14	12	1	14	12	0	14	13	2
14	13	1	14	13	0	14	14	3	14	14	2
14	14	1	14	14	0	14	15	3	14	15	2
14	15	1	14	15	0	14	16	3	14	16	2
14	16	1	14	16	0	14	17	2	14	17	1
14	17	0	14	18	2	14	18	1	14	18	0

14	19	2	14	19	1	14	19	0	14	20	2
14	20	1	14	20	0	15	11	0	15	12	1
15	12	0	15	13	1	15	13	0	15	14	2
15	14	1	15	14	0	15	15	3	15	15	2
15	15	1	15	15	0	15	16	3	15	16	2
15	16	1	15	16	0	15	17	3	15	17	2
15	17	1	15	17	0	15	18	3	15	18	2
15	18	1	15	18	0	15	19	3	15	19	2
15	19	1	15	19	0	15	20	3	15	20	2
15	20	1	15	20	0	16	11	0	16	12	0
16	13	1	16	13	0	16	14	2	16	14	1
16	14	0	16	15	3	16	15	2	16	15	1
16	15	0	16	16	3	16	16	2	16	16	1
16	16	0	16	17	3	16	17	2	16	17	1
16	17	0	16	18	3	16	18	2	16	18	1
16	18	0	16	19	3	16	19	2	16	19	1
16	19	0	16	20	3	16	20	2	16	20	1
16	20	0	17	12	0	17	13	0	17	14	1
17	14	0	17	15	2	17	15	1	17	15	0
17	16	3	17	16	2	17	16	1	17	16	0
17	17	4	17	17	3	17	17	2	17	17	1
17	17	0	17	18	4	17	18	3	17	18	2
17	18	1	17	18	0	17	19	3	17	19	2
17	19	1	17	19	0	17	20	3	17	20	2
17	20	1	17	20	0	18	13	0	18	14	1
18	14	0	18	15	1	18	15	0	18	16	2
18	16	1	18	16	0	18	17	3	18	17	2
18	17	1	18	17	0	18	18	4	18	18	3
18	18	2	18	18	1	18	18	0	18	19	4
18	19	3	18	19	2	18	19	1	18	19	0
18	20	4	18	20	3	18	20	2	18	20	1
18	20	0	19	13	0	19	14	0	19	15	1
19	15	0	19	16	2	19	16	1	19	16	0
19	17	3	19	17	2	19	17	1	19	17	0
19	18	3	19	18	2	19	18	1	19	18	0
19	19	4	19	19	3	19	19	2	19	19	1
19	19	0	19	20	4	19	20	3	19	20	2
19	20	1	19	20	0	20	14	0	20	15	1
20	15	0	20	16	1	20	16	0	20	17	2
20	17	1	20	17	0	20	18	3	20	18	2
20	18	1	20	18	0	20	19	4	20	19	3
20	19	2	20	19	1	20	19	0	20	20	5

20	20	4	20	20	3	20	20	2	20	20	1
20	20	0	-	-	-	-	-	-	-	-	-

Table A.1: Table of all combinations of m, s, and L which are type 1 anomalous sequences of ${}_sA_{\ell m}$

Appendix B: List of Type 2 Anomalous Lines

The following table is a list of all type 2 anomalous sequences found in this study. These anomalous sequences all have some form of deflection behavior similar to that seen in Fig. 2.8, have oscillatory behavior of order $|c|^{-1}$ shown in Fig. 5.4, and only follow the polynomial power-series expansion given in Eq. (5.1) after making the shift of $L \to L^* = {}_sN_{\ell m}$.

m	s	L	m	s	L	m	s	L	m	s	L
2	2	1	2	3	3	2	4	5	2	5	8
2	6	12	2	7	16	3	7	1	3	8	1
3	9	1	3	10	2	3	11	2	3	12	3
3	13	3	3	14	4	3	15	4	3	16	5
3	17	5	3	18	6	3	19	7	3	20	7
4	3	9	4	17	1	4	18	1	4	19	1
4	20	1	5	5	3	5	6	5	5	7	7
5	8	10	5	9	13	5	10	17	5	11	20
6	8	2	6	9	3	6	10	4	6	11	5
6	12	6	6	13	7	6	14	8	6	15	9
6	16	10	6	17	12	6	18	13	6	19	14
6	20	16	7	5	3	7	6	8	7	7	16
7	12	2	7	13	2	7	14	3	7	15	3
7	16	4	7	17	4	7	18	5	7	19	5
7	20	6	8	7	2	8	8	5	8	9	7
8	10	9	8	11	12	8	12	15	8	13	18
8	14	21	8	17	2	8	18	2	8	19	2
8	20	2	9	6	8	9	7	20	9	9	3
9	10	3	9	11	4	9	12	5	9	13	7
9	14	8	9	15	9	9	16	11	9	17	12
9	18	14	9	19	15	9	20	22	10	7	1
10	8	5	10	9	10	10	10	15	10	11	20

10	13	3	10	14	4	10	15	4	10	16	5
10	17	6	10	18	6	10	19	7	10	20	8
11	7	17	11	9	2	11	10	5	11	11	7
11	12	9	11	13	12	11	14	14	11	15	17
11	16	3	11	16	20	11	17	3	11	17	23
11	18	3	11	18	25	11	19	4	11	20	4
12	8	4	12	9	10	12	10	18	12	11	3
12	12	5	12	13	6	12	14	7	12	15	8
12	16	9	12	17	11	12	18	12	12	19	14
12	20	23	13	9	1	13	10	4	13	11	8
13	12	12	13	13	17	13	14	4	13	14	21
13	15	4	13	15	25	13	16	5	13	17	6
13	18	7	13	19	8	13	20	8	14	9	8
14	10	18	14	11	2	14	12	4	14	13	7
14	14	10	14	15	12	14	16	14	14	17	4
14	17	16	14	18	4	14	18	19	14	19	5
14	19	22	14	20	5	14	20	24	15	10	2
15	11	7	15	12	13	15	13	3	15	13	19
15	14	4	15	14	27	15	15	7	15	16	8
15	17	9	15	18	10	15	19	12	15	20	13
16	10	14	16	12	3	16	13	7	16	14	10
16	15	14	16	16	5	16	16	19	16	17	6
16	17	22	16	18	6	16	18	26	16	19	7
16	19	30	16	20	8	17	11	5	17	12	12
17	13	2	17	13	27	17	14	4	17	15	7
17	16	9	17	17	12	17	18	14	17	19	5
17	19	16	17	20	5	17	20	19	18	12	2
18	13	6	18	14	10	18	15	3	18	15	15
18	16	4	18	16	21	18	17	6	18	17	26
18	17	31	18	18	9	18	19	10	18	20	11
19	12	9	19	13	18	19	14	3	19	15	6
19	16	9	19	17	13	19	18	5	19	18	17
19	19	7	19	20	8	19	20	34	20	13	3
20	14	9	20	15	15	20	16	4	20	16	22
20	17	6	20	17	32	20	18	9	20	19	12
20	20	14	-	-	-	-	-	-	-	-	-

Table B.1: List of all combinations of m, s, and L which lead to type 2 anomalous sequences of ${}_sA_{\ell m}$

Curriculum Vitae : Daniel J. Vickers

Educational Background

- Undergraduate : Wake Forest University

  BS Physics, BA Mathematics, Minor Chemistry

  GPA : 3.78, Magna Cum Laude

  Honors Thesis: Determining the Asymptotic Expansion of Prolate Spin-Weighted Spheroidal Eigenvalues

- Masters : Wake Forest University

  MS Physics

  GPA : 3.66

Academic Awards

Recipient of the WFU Teaching Assistant Award 2019

Skills

- Programming: Java, Python, C#, C++, JavaScript, mySQL, Node.js, Flask, MATLAB, vPython, numPy, SciPy
- Software : Git, Unity, Mathematica

Publications

Gregory B. Cook, Luke S. Annichiarico, and Daniel J. Vickers. Unknown branch of the total-transmission modes for the Kerr geometry. *Phys. Rev. D*, 99:024008, Jan. 2019.